A COMPUTATIONAL INVESTIGATION OF A LOBED-MIXER FUEL-INJECTION STRUT IN A SCRAMJET ENGINE MODEL

by

MARIO FELIPE CAMPUZANO

B.S. in Mechanical Engineering, State University of New York at Buffalo, 1994

B.S. in Aerospace Engineering, State University of New York at Buffalo, 1994

THESIS

Submitted in partial fulfillment of the requirements for the
degree of Master of Science in Mechanical Engineering
in the Graduate School of Syracuse University

May 1997

Approved _____

Dr. Thong Q. Dang

Date _____

Abstract

A method of enhancing fuel/air mixing using streamwise vorticity for scramjet applications is presented. The generation of large-scale streamwise vortices is achieved by the incorporation of a lobed-mixer device into the fuel-injection struts of a proposed NASA scramjet engine. Conceptually, the lobed-mixer strut design is a three-dimensional lifting surface with a sinusoidal spanwise lift distribution. In the flow passage between the strut leading- and trailing-edges, the presence of a spanwise pressure gradient generates secondary flows. In the region behind the strut, which is a lifting surface, the shed vorticity system consists of periodic large-scale counter-rotating streamwise vortices. To evaluate this hypermixer concept, CFD calculations were carried out at supersonic combustor inlet Mach numbers ranging from 2 to 3 for cold flows.

This concept is first analyzed for a 3D cascade of struts in inviscid flows. Results from this preliminary work reveal that significant secondary flows are generated in and behind the strut regions, while the additional shock losses associated with the lobed strut is small. Results confirm that the mechanism of generating streamwise vorticity is an inviscid phenomenon; the shed vorticity (i.e. streamwise vorticity) behind the strut is proportional to the pressure loading along the strut (Kutta-Joukowsky theorem).

The next stage of this investigation considers the effects of viscosity on the generation of streamwise vorticity (or secondary flow). The geometry considered is a single lobed strut with "slip" side walls. Here, the NASA Reynolds-Averaged Navier-Stokes LARCK code (Langley Algorithm for Research in Chemical Kinetics) was used. Relative to the inviscid-flow results, in the absence of flow separation, viscous effects

introduce blockage into the flow passage, causing a small reduction in pressure loading and hence a slight reduction in secondary flow. In the presence of flow separation, the strut pressure loading can be significantly reduced, resulting in a large reduction in secondary flow.

Next, the effect of Mach number on the strength of the streamwise vorticity is investigated. For the configuration studied, the pressure loading along the strut (hence the magnitude of secondary flow) was found to be a strong function of the strength and angle of the leading-edge shocks, which depends on the inflow Mach number.

Finally, preliminary experimental verification of this hypermixer concept was carried out. Flow visualizations confirm the presence of strong large-scale streamwise vortices downstream of the strut.

Acknowledgments

I would like to thank my advisor, Prof. Thong Q. Dang, who not only was responsible for my success in graduate school and undergraduate research, but also encouraged me to study and solve challenging technical problems.

I sincerely wish to thank the National Aeronautics and Space Administration (NASA) for awarding me a training grant to complete my graduate studies. NASA's support was critical to my success in graduate school, and my gratitude to the agency is enormous. My special thanks also go to my advisors at the NASA Langley Research Center, Mr. Griffin Y. Anderson and Dr. J. Phillip Drummond, both of the Hypersonic Airbreathing Propulsion Branch, for providing me with the tools and advise to complete my research while my tenure at the Center. Many thanks to Mr. Jeffery A. White for his advice with matters related to the LARCK code and to the Office of Education at the Langley Research Center for their support, specially to Mr. Lloyd Evans and Mr. Roger A. Hathaway. Finally, I would like to acknowledge Prof. D. Papamoschou at UCI for giving me permission to include the experimental results in the thesis.

A final thanks to the Department of Mechanical, Aerospace, and Manufacturing Engineering at Syracuse University for accepting me into their graduate program and for providing me with quality education, and to the members of my thesis defense committe for their time.

Contents

List of Tables

List of Figures

Nomenclature

β	Camber angle distribution function
β_o	Camber angle at the trailing edge
c	Strut chord
D	Stream thrust loss ratio
δ	Boundary layer thickness
ϵ	Lobe ramp angle
Γ_{sec}	Secondary flow circulation
Γ_{strut}	Maximum strut sectional circulation
H	Height of the strut
λ	Lobe wavelength
Ω_s	Streamwise vorticity
Ω_x	Axial vorticity
p_{dist}	Static pressure distortion indicator
p_{max}	Maximum static pressure at outlet
p_{min}	Minimum static pressure at outlet
P_o	Stagnation pressure
σ	Control variable for lobe trailing edge shape
t_{max}	Strut maximum thickness
s	Blade spacing for cascade cases
$\bar{V}$	Momentum-averaged velocity
ΔP_0	Momentum-averaged stagnation pressure loss
θ	Angle between streamline and axial coordinate x

Chapter 1

Introduction

The basic scramjet engine uses a series of fixed-geometry rectangular scramjet modules that are mounted side-by-side and are integrated with the airframe [21]. The integration of the vehicle and the propulsion system takes advantage of forebody compression to reduce inlet size, and aftbody expansion to provide a low-drag, high-area-ratio exhaust nozzle. Figure 1.1 shows the scramjet concept studied at NASA Langley. In this design, after the incoming airstream is precompressed by the forebody, the inlet of the engine module further compresses the incoming flow with swept wedge-shaped side walls. Finally, the engine compression process is completed by wedge-shaped struts that also provide locations for injection of gaseous fuel. Along the aft portion of these struts (typically at midchord and at the trailing edge), gaseous fuel is injected normally and/or tangentially into the airstream, depending on the flight speed. The fuel and air mix and react in the combustor portion of the module, and the reacted mixture is then expanded through the nozzle.

Since the development of this basic NASA engine design, a number of modified designs have been developed that retain the basic features of the original design. For the inlet portion of the scramjet engine, new developments include two-strut inlets [11], reverse sweep inlets [12], and translating strut inlets [18]. In the combustor portion of the scramjet engine, normal and tangential fuel ports are strategically employed and placed along the walls and struts to maximize fuel/air mixing for the combustion process, and minimize shock losses and high local heating [5, 14].

1
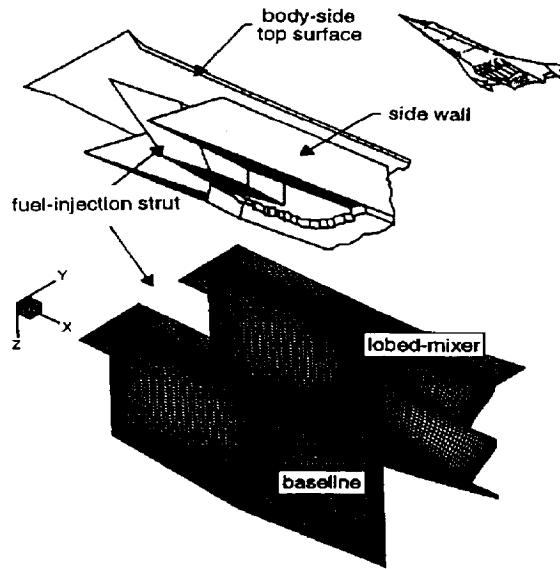
Figure 1.1: NASA scramjet engine concept.

In the typical flight envelope of a hypersonic vehicle, various combustor fuel injection systems have been investigated for different speed ranges and flow conditions. In the low Mach number flight regime, fuel can be injected normal to the airstream to maximize fuel penetration into the airstream. As the vehicle transitions to high Mach number, the fuel ports are changed from normal injection to parallel injection. The latter strategy is employed to reduce the large shock losses associated with the detached normal shock wave upstream of the normal fuel jet, and to utilize the fuel axial momentum flux to generate thrust.

The flow physics associated with parallel fuel injection can be studied by the 2D mixing layer model. In a subsonic mixing layer, the growth rate of a mixing layer is controlled by the large-scale organized vortical structures that are initiated by the Kelvin-Helmholtz instability [2]. These large-scale coherent structures are responsible for the bulk mixing (or momentum transport), while small-scale mixing is related to the presence of fine-scale turbulence in the mixing layer. As the convective Mach number increases it has been observed that the mixing layer becomes stable,

and the large-scale structures become nearly indiscernible. As a result, the growth rate of the mixing layer is dramatically reduced [15]. The effect of this decreased mixing rate at high Mach numbers is compounded by the extremely short scramjet combustor-residence time. To counteract these detrimental effects, both active and passive flow-control techniques have been proposed to enhance the mixing rate in supersonic mixing layers [7, 10]. Typical techniques that provide augmentation of large-scale and molecular mixing include dynamic fuel injection, proper imposition of pressure difference across the mixing layer, shock/mixing-layer interactions, shock oscillations, and streamwise vorticity injection.

In this work, we propose a technique of enhancing mixing via streamwise vorticity generation by a lobed mixer strut. The hypermixer fuel-injection strut presented here can be incorporated into the basic NASA Langley scramjet engine concept. Figure 1.1 illustrates the baseline strut design and the new lobed-mixer strut design investigated in this study. The baseline design can be modeled as a straight strut, which are wedge-shaped cross sections in the z-direction. The forward half of the diamond-shaped strut constitutes the last compression stage in the engine, while fuel is injected over the aft half of the strut.

In the new lobed-mixer strut, the forward portion of the strut is the same as in the baseline configuration, and the aft portion of the lobed-mixer strut is constructed using a "lobed" surface. The lobed-mixer strut is constructed from a prescribed camber surface and thickness distribution. The camber surface of the lobed-mixer strut can be characterized by (1) a chordwise (x-direction) camber variation, and (2) a spanwise (z-direction) camber-angle variation at the trailing edge. The chordwise camber variation is generated from a prescribed linear variation in camber angle, while the trailing-edge camber-angle variation is controlled using a sinusoidal function. The lobed-mixer geometry is generated using the following camber-angle distribution:

$$
\beta(x, z) = \begin{cases} 0 & 0 \le x \le \frac{1}{2} \\ \beta_0 (cos\frac{2\pi\lambda z}{H})^\sigma (2x - 1) & \frac{1}{2} \le x \le 1 \end{cases}
$$

where H is the height of the strut. In the above expression, β_0 is the maximum camber

angle at the trailing edge and is used to control the lobe height. The parameter λ is used to control the number of lobes (or the lobe wavelength), while the parameter σ is used to control the shape of the trailing edge. Finally, the strut thickness distribution is taken to be that of a wedge with a maximum thickness-to-chord ratio of 9.6% (corresponding to a half-wedge angle of 5.5°).

The proposed fuel-injection strut promotes rapid fuel/air mixing via a lobed-mixer device [19] which injects an array of large-scale streamwise vortices into the flowfield. The new strut design is derived from the forced-mixer nozzle technology used in conventional turbofan engines [19]. It has been experimentally verified that these lobed nozzles efficiently mix the hot stream leaving the core engine and the cold stream leaving the fan [16, 20]. At the present time lobed-mixer devices have been used successfully in operational aircraft engines. The goal of this study is to perform a preliminary evaluation of the mixing enhancement ability and the resulting drag penalty of the lobed-mixer strut for a variety of configurations in cold (non-reacting) flows.

A promising engine in which the lobed-mixer concept can also be incorporated into is the Aerojet Strutjet Engine shown in figure 1.2 [3]. The Strutjet inlet is based on the NASA Langley sidewall compression inlet (see top section of figure 1.1), and the struts are integrated into the inlet section such that each flow passage between two struts behaves like the original Langley engine with sidewall compression. The strutjet design provides the optimum combination between rocket and airbreathing propulsion for maximizing vehicle performance and minimizing vehicle operating costs. Essentially five operating modes are available in the strutjet engine:

- Mode 1. As a ducted rocket from launch to Mach 2.5.

- Mode 2. As a ramjet from flight Mach number 2.5 to 5.

- Mode 3. As a scramjet from Mach 5 to 8.

- Mode 4. As a dual mode scram/rocket during flight in the outer regions of the atmosphere above Mach 8.
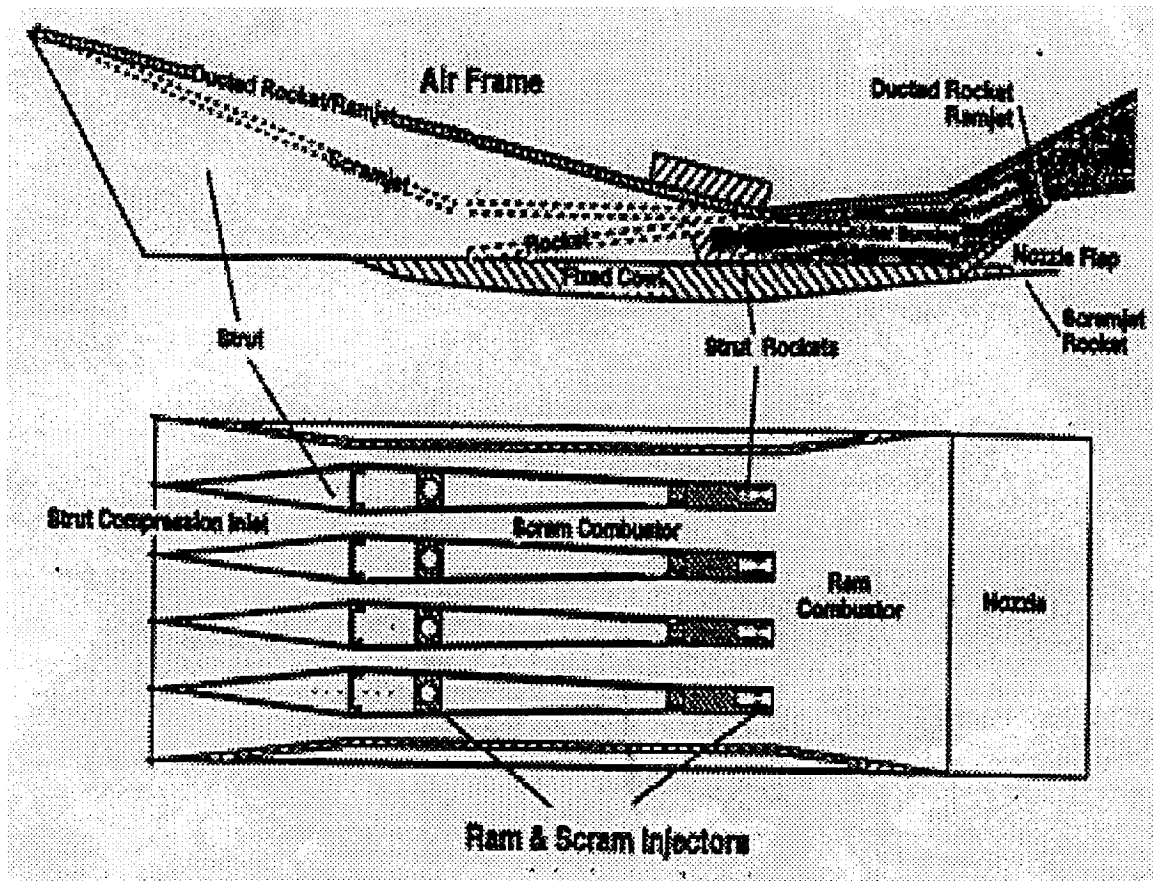
Figure 1.2: Strutjet - The integration of a rocket into a ramjet combining the benefits of both (Ref. 3).

- Mode 5. As a conventional rocket outside the atmosphere.

In the airbreathing operational mode, the struts also serve as locations for fuel injectors. Figure 1.3 [3] displays the advantages of the strutjet over an strutless engine. It shows that for a mixing gap ratio G/g of three, the length of the combustor can be reduced by a factor of 3. Hence, the size and weight of the combustor can be greatly reduced if the strutjet engine is used instead of the strutless engine. To give a rough idea about the size of the combustor required for the strutjet, combustion efficiencies of 95% have been experimentally demonstrated with hydrocarbon fuels at Mach 8 flight conditions at less than 50 inches downstream from the fuel injector location, and
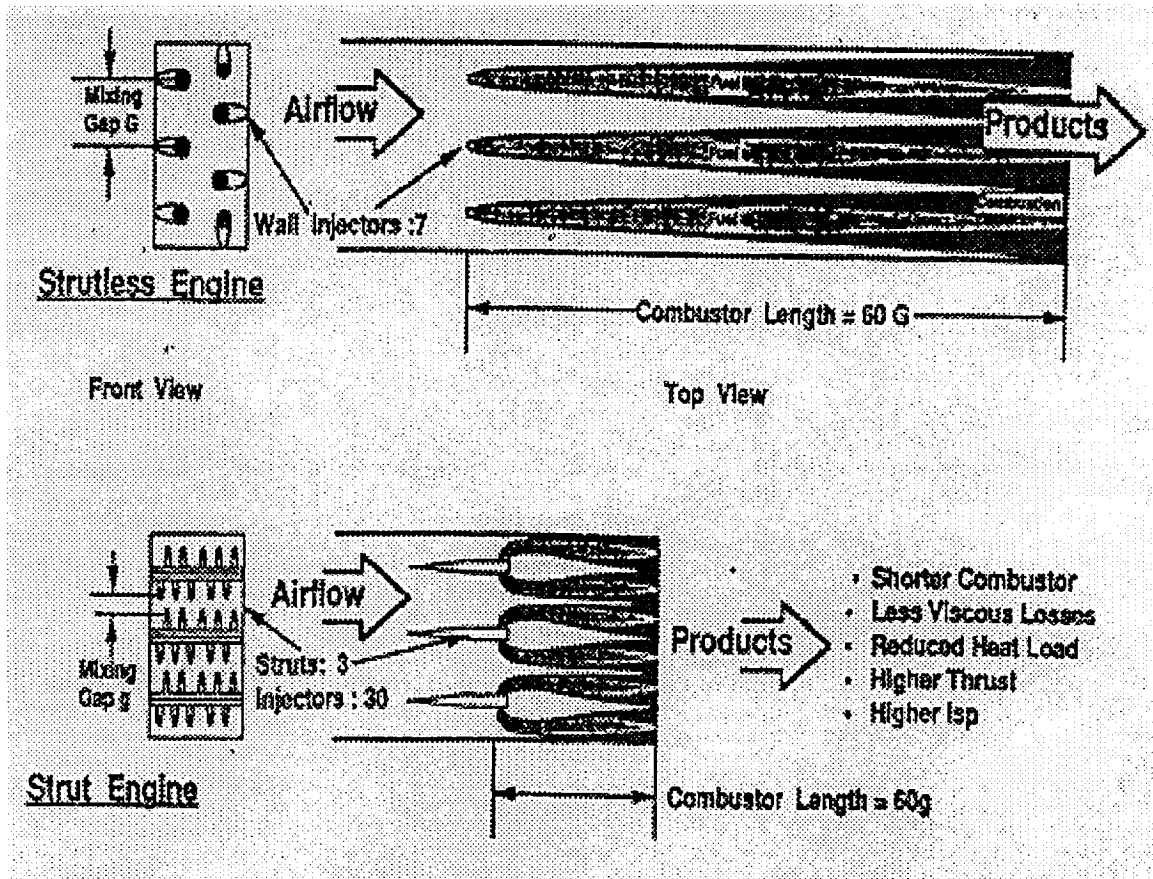
Figure 1.3: Comparison of Strutjet and Strutless engines (Ref. 3).

about 90% at 30 inches from the injection location. Besides of serving as primary fuel injector locations the Aerojet engine struts are also key elements providing multiple operational functions such as compression of incoming air, inlet/combustor isolation and rocket thruster integration.

Chapter 2

Cascade Strut - Proof of Concept

In this section computations have been performed to test the hypothesis that the lobed-mixer concept can be effectively applied to a hypersonic scramjet engine. In this initial study, a three-dimensional cascade of struts has been used to model two configurations: a cascade of baseline struts and a cascade of lobed-mixer struts. The aspect ratio ($H/c = 0.5$), maximum thickness-to-chord ratio ($t_{max}/c=0.096$), and spacing-to-chord ratio ($s/c=0.24$) are representative of the NASA Langley engine configuration [11]. The lobed-mixer geometry is generated using Eq. (1) with the following parameters: $\beta_0=12°$, $\lambda=2$, and $\sigma=1$. This lobed-mixer design has similar overall geometrical dimensions as the UTRC Low Penetration Mixer (LPM) investigated at low speed ($M_\infty = 0.1$) [19]. The lobed-mixer studied here has a lobe height-to-wavelength ratio of 0.25 and an equivalent ramp angle of 5.8°. However, the chordwise camber distribution in the present design is different from the UTRC LPM configuration. A design similar to the LPM configuration is studied here since choking and shock losses associated with the presence of the lobes are issues of concern in high Mach-number flows. Figure 2.4 illustrates the baseline and lobed-mixer struts studied here.

As the essential physics of the lobed-mixer are captured by an inviscid-flow model [1, 6, 19], a three-dimensional Euler code developed for turbomachine flowfield calculations has been employed to evaluate these two designs. The Euler solver employs the finite-volume Runge-Kutta time-stepping algorithm of Jameson et al. [8]. The

standard second- and fourth-difference dissipations developed for transonic flows are employed here. Consequently, the code employed here is not the code-of-choice for this application. In the calculations presented in this paper, an H-mesh with 176 x 28 x 60 cells was used. The farfield station is placed at 50% chord downstream of the strut's trailing edge (or 8 lobe heights). The incoming Mach number is taken to be 3. In the results presented here, all length scales are normalized by the strut axial chord c, velocity scales are normalized by $\sqrt{RT_{0\infty}}$, and pressure scales are normalized by $P_{0\infty}$. At the freestream Mach number of 3, the normalized freestream velocity is 2.1.

Conceptually, the lobed-mixer strut design is a three-dimensional lifting surface with a sinusoidal spanwise distribution of loading (or circulation). In the flow passage between the struts, the presence of a spanwise pressure gradient $\partial p / \partial z$ along the strut generates secondary flows (Fig. 2.4). Figure 2.5 shows contour plots of the z-component of velocity on the surfaces of the baseline and lobed-mixer struts. This figure shows that the magnitude of the normalized secondary flow velocity is up to 0.2 (or 10% of the freestream velocity). This value compares very well with the experimental results reported by Skebe et al. [19] for the LPM configuration, in spite of the large difference in the inflow Mach number.

Figures 2.4 and 2.5 clearly indicate that the baseline flowfield is highly two-dimensional (V_z is negligible), while the lobed-mixer flowfield is very three-dimensional (V_z is substantial). If fuel were to be injected along the strut at the midchord location, the large-scale secondary flow motions would sweep the fuel toward the airstream and enhance mixing and combustion.

In the region behind the strut, the presence of the trailing vortex sheet (e.g. streamwise vorticity) in the lobed-mixer configuration will further enhance the mixing of fuel and air. Figure 2.6 shows the secondary flow velocity vectors at three axial stations in the downstream region behind the lobed-mixer strut (104%, 122% and 150% chord from the leading edge). This figure clearly shows the presence of large-scale counter-rotating streamwise vortices in the downstream region. The figure indicates that the secondary-flow velocity is concentrated at the inviscid wake

near the trailing edge and diffuses through the flow domain with downstream distance. The diffusion of the secondary-flow velocity is primarily due to the presence of artificial viscosity in the present algorithm.

Figure 2.7 illustrates the locations of the wake (or trailing-vortex sheet) at these three axial locations for the lobed-mixer design. Again, the presence of artificial viscosity and the quality of the mesh have resulted in the spreading of the inviscid wake with downstream distance. However, this figure does indicate that there are significant movements of the wake toward the middle of the flow passage and a large increase in interfacial area between the streams. This figure implies that if fuel is injected at the trailing edge of the strut, it will have significantly penetrated into the flow passage by one-half chord-length downstream of the strut.

In the design of hypermixer configurations, it is important to recognize that mixing enhancement will lead to a drag penalty, and a balance between these must be achieved. The objective is to design a lobed-mixer strut geometry that causes the fuel to penetrate the air stream in the shortest distance possible while minimizing the loss in stream thrust. The use of the lobed-mixer strut for enhanced fuel/air mixing can result in an increase in losses relative to the baseline strut because the secondary-flow kinetic energy does not contribute to thrust, and additional shock waves can appear in the flow passage. Figure 2.8 illustrates a comparison of the flowfields on a constant z-plane between the baseline and lobed-mixer struts. Here, the midspan z-plane is chosen where the lobed-mixer strut has the highest camber. As expected, the flowfield in the forward half of the two struts are identical. In the rear half of the struts, we observe that the two flowfields are not significantly different. In particular, the compression and expansions processes along the lobed-mixer surfaces appear to be isentropic. This can be seen from the plot of the Mach number distributions along the strut surfaces shown in Fig. 2.9. The difference in the shock loss between the two designs is in the strength of the trailing-edge shock system.

Figure 2.10 illustrates the entropy contours on the same spanwise plane. These contour plots reveal the entropy rise across the leading-edge shock, the impinging/reflected shock along the strut surfaces at the midchord location, and the trailing

edge shock system. The figure reveals that the overall level of entropy rise between the two designs are roughly the same, indicating that additional shock losses generated in the lobed-mixer design are not significant.

In order to quantify the mixing "goodness" and the drag penalty associated with the proposed lobed-mixer design, several global parameters are defined to aid this evaluation task. The parameters used to quantify mixing goodness are [9]:

(1) Momentum-averaged spanwise velocity $\bar{V_z}$ evaluated on a constant axial plane (normalized to $\sqrt{RT_{0\infty}}$)

$$\bar{V_z}(x) \equiv \frac{\int\int |V_z|(\rho V_x^2 dy dz)}{\int\int (\rho V_x^2 dy dz)} \tag{2.1}$$

This quantity is used to measure the intensity of 3D effects in the flowfield.

(2) Momentum-averaged crossflow velocity $\bar{V}_{yz}$ evaluated on a constant axial plane (normalized to $\sqrt{RT_{0\infty}}$)

$$\bar{V}_{yz}(x) \equiv \frac{\int\int \sqrt{V_y^2 + V_z^2}(\rho V_x^2 dy dz)}{\int\int (\rho V_x^2 dy dz)} \tag{2.2}$$

This quantity is a good measure of the secondary-flow velocity magnitude in the downstream region.

(3) Secondary-flow circulation Γ_{sec} evaluated on a constant axial plane (normalized to $c\sqrt{RT_{0\infty}}$)

$$\Gamma_{sec}(x) \equiv \int\int |\Omega_x| dy dz \tag{2.3}$$

In the strut region, the integration path encloses the flow passage. In the downstream region, the integration path includes the vortex sheet. The secondary-flow circulation Γ_{sec} represents the total flux of axial vorticity (absolute value) through a constant axial plane.

(4) Maximum strut sectional circulation Γ_{strut} (normalized to $c\sqrt{RT_{0\infty}}$)

$$\Gamma_{strut} \equiv \left| \int_{outlet} V_y dy \right|_{max} \tag{2.4}$$

Here, the integration path is taken on the xy plane enclosing the strut and chosen at the spanwise location where the magnitude of the circulation is largest (Fig. 2.11). For a lobed-mixer strut of infinite length in the spanwise direction (i.e. in the absence of the upper and lower boundaries), one can model the lobed-mixer strut and the wake as periodic bound- and shed-vortex systems (Fig. 2.11). If there is no vorticity-generation mechanism in the flowfield and no vortex merging in the downstream region, it is readily verified that, behind the strut trailing edge, Γ_{sec} is constant and takes on the value

$$\Gamma_{sec} = 4\lambda\Gamma_{strut} \tag{2.5}$$

To promote rapid mixing, the above parameters should be maximized.

The parameters used to quantify the drag penalty are:

(1) Stream thrust loss ratio D

$$D \equiv \frac{\int\int_{outlet}(\rho V_x{}^2 + p)dydz - \int\int_{inlet}(\rho V_x{}^2 + p)dydz}{\int\int_{inlet}(\rho V_x{}^2 + p)dydz} \tag{2.6}$$

(2) Momentum-averaged stagnation pressure loss ΔP_0 evaluated on a constant axial plane

$$\Delta P_0(x) \equiv 1 - \frac{\int\int (P_0/P_{0\infty})(\rho V_x^2 dydz)}{\int\int (\rho V_x^2 dydz)} \tag{2.7}$$

(3) Static pressure distortion indicator p_{dist} at the outflow boundary

$$p_{dist} \equiv \left(\frac{p_{max}}{p_{min}}\right)_{outlet} \tag{2.8}$$

To keep the loss low, the parameters D and ΔP_0 should be minimized. The static pressure distortion indicator p_{dist} should be kept near unity so that the flow leaving the combustor is uniform.

Figures 2.12 and 2.13 show the axial distributions of the momentum-averaged spanwise velocity $\bar{V}_z$ and crossflow velocity $\bar{V}_{yz}$, respectively, for the baseline and lobed-mixer struts. From the leading edge to the 60% chord location, the baseline

and lobed-mixer struts have the same $\bar{V}_{yz}$ distribution and no momentum-averaged spanwise velocity. In this region, the two flowfields are nearly two-dimensional, and the crossflow velocity is composed primarily of the transverse or y-component velocity acquired by the flow as it crosses the oblique shock system. Hence, it is not the secondary flow that can assist mixing.

As the flow proceeds downstream from the 60% chord location, the axial distributions of $\bar{V}_z$ and $\bar{V}_{yz}$ between the baseline and lobed-mixer struts start to deviate. Figure 2.12 shows that the spanwise velocity is zero in the case of the baseline configuration, indicating that the flow is two-dimensional. On the other hand, the spanwise velocity is significant for the lobed-mixer configuration, indicating that the flow is three-dimensional. Figure 2.13 shows that the crossflow velocity is reduced significantly in the baseline configuration, while its amplitude is on the order of 0.18 (or 10% of the freestream velocity) in the lobed-mixer configuration. The difference in crossflow velocity between the baseline and lobed-mixer curves represents secondary flows that can be used to promote rapid mixing.

Figure 2.14 shows the axial distributions of the secondary-flow circulation Γ_{sec} for the baseline and lobed-mixer struts in the flow passage and in the downstream region. The figure shows that the baseline configuration has zero axial vorticity, as expected. On the other hand, the lobed-mixer strut generates some axial vorticity in the flow passage, and the sudden jump in Γ_{sec} at the trailing edge represents the contribution of circulation from the trailing vortex sheet.

The magnitude of Γ_{sec} in the strut region is small and is on the order of 10% of the value in the downstream region. The generation of axial vorticity in the strut region is not in violation with Kelvin's theorem for inviscid flows. Here, although the incoming flow is irrotational, the flow in the strut region is rotational. The generation of entropy gradient behind the oblique shock structure in the forward portion of the strut produces some spanwise vorticity Ω_z (Fig. 2.10), and the presence of a three-dimensional velocity field can tilt/distort these spanwise vortex lines and introduces axial vorticity. Since the present numerical algorithm contains artificial viscosity, the entropy gradient produced in the flowfield is not entirely due to the shock waves.

In the downstream region, Fig. 2.14 indicates that the magnitude of the secondary-flow circulation is on the order of 0.41. In the work reported by Skebe et al. [19], it was shown that the secondary-flow circulation can be approximated as, for a half-wavelength lobe,

$$\Gamma = C_1 a U_\infty tan(\epsilon)$$ (2.9)

In the above relation, a is the lobe height, and ϵ is the lobe ramp angle. The theoretical value for the constant C_1 is 2.5, while the experimental value for the UTRC LPM configuration is 3.3 [19]. Since the value for Γ_{sec} in Fig. 2.14 is for two full lobes, Eq. (10) can be expressed as

$$\frac{\Gamma_{sec}/4}{c\sqrt{RT_{0\infty}}} = C_1 \frac{a}{c} \frac{U_\infty}{\sqrt{RT_{0\infty}}} tan(\beta_0)$$ (2.10)

In the above expression, the strut trailing edge angle β_0 was used as the lobe ramp angle. In the present problem, the ratio (a/c) is 0.052, and the non-dimensional freestream velocity $U_\infty/\sqrt{RT_{0\infty}}$ is 2.1. Using the value 0.41 for Γ_{sec} taken from Fig. 2.14, it is found that C_1 is 4.4, which is higher than the the results of Skebe et al. [19]. Finally, the calculated value for the maximum strut sectional circulation Γ_{strut} is 0.048. This gives $(4\lambda\Gamma_{strut})/(\Gamma_{sec}) = 0.94$, which is very close to the theoretical value of 1 given in Eq. (6). The difference between these two values represents vorticity generation in the flowfield due to the presence of shock waves and numerical dissipation.

Figure 2.15 shows the axial distribution of the momentum-averaged stagnation pressure loss ΔP_0 for the baseline and lobed-mixer struts. This figure reveals that the magnitudes of the stagnation pressure loss associated with the shock structures in the strut region between the two designs are nearly the same and are on the order of 2.8%. In the downstream region, the rise in stagnation pressure loss is higher for the lobed-mixer strut than the baseline strut, by about an additional 1%. The rise in stagnation pressure loss in the downstream region is due to the presence of (1) the trailing-edge shock (Fig. 2.9), and (2) numerical diffusion of the trailing vortex sheet

(like a mixing loss). Finally, calculation of the stream thrust loss D yields a value of -0.31% for the baseline design and -0.77% for the lobed-mixer design. This represents a relatively small drag penalty for the gain in secondary flows.

2.1 Parametric Study

The preliminary results presented in the previous section are very encouraging; they indicate that the proposed lobed-mixer design generates significant secondary flows for enhanced fuel/air mixing while the increase in stream thrust loss is small. In this section, a parametric study is carried out as a function of the lobed-mixer geometrical parameters $(\beta_0, \lambda, \sigma)$.

2.1.1 Influence of lobe height (varying β_0)

Here the performance comparison between the baseline design and three lobed-mixer struts is presented, having values for β_0 as $6°$, $12°$, and $18°$. The case with a low value for β_0 corresponds to a low penetration lobed-mixer (a/c=0.026), while the case with a large values of β_0 corresponds to a higher penetration lobed-mixer (a/c=0.076). The parameters λ is set to 2, while the parameter σ is set to 1. This geometry corresponds to a two-lobe strut with a smoothly varying sinusoidal trailing edge shape.

Figures 2.16 and 2.17 illustrate the secondary velocity vectors and the location of the wake at the outflow axial stations, respectively. As expected, the secondary flowfield is a strong function of β_0. The strut with the highest value of β_0 has the highest secondary-flow magnitude and the highest level of wake distortion relative to the trailing edge shape.

Table 1 summarizes the performance parameters obtained from the numerical results. This table shows that the parameters $(\bar{V}_{yz}, \Gamma_{sec}, \Gamma_{strut})$ measuring mixing goodness and the parameters (D, ΔP_o) measuring drag penalty are strong functions of β_0. We note that the values of C_1 in Eq. (11) decreases with β_0 (or lobe height), which is consistent with the experimental results of Skebe et al. [19]. The numerical

results of Γ_{sec} and Γ_{strut} agree well with the theoretical relation given in Eq. (6).

In terms of drag penalty, the stream thrust loss in the baseline design is 0.31%, while the stream thrust loss in the lobed-mixer struts studied here ranges from 0.43% to 1.3%. Finally, the static pressure distortion indicator (p_{dist}) is of the same order of magnitude in the three lobed-mixer struts and is roughly 25% higher than the baseline strut.

2.1.2 Influence of number of lobes (varying λ)

Here the performance comparison between the baseline design and three lobed-mixer struts is presented, having values for λ as 1, 2, and 3. The parameters β is set to 12°, while the parameter σ is set to 1. This geometry corresponds to a 12°-camber strut with a smoothly varying sinusoidal trailing edge, and the number of lobes is proportional to λ.

Figures 2.18 and 2.19 illustrate the secondary velocity vectors and the location of the wake at the outflow axial stations, respectively. It is observed that the magnitude of the secondary-flow velocity and the degree of wake distortion decreases with increasing value of λ. This is seen from the magnitude of $\bar{V}_{yz}$ and Γ_{strut} given in Table 2. On the other hand, Table 2 shows that Γ_{sec} increases with increasing value of λ. This is due to the fact that, eventhough the $\lambda=1$ strut has the highest sectional circulation, the number of counter-rotating streamwise vorticity pairs is proportional to λ (or the number of lobes). It is noticed that the values of C_1 in Eq. (11) increases with λ, which cannot be prediced by the theoretical result given in Eq. (11). Again, the numerical results of Γ_{sec} and Γ_{strut} agree well with the theoretical relation given in Eq. (6). In terms of mixing goodness, Fig. 2.19 indicates that the single-lobe strut pushes the fuel farther into the main flow than the multiple-lobe mixer strut. However, the multiple-lobe mixer spreads the fuel out more evenly than the single-lobe mixer.

In Table 2, the parameters measuring drag penalty shows that the magnitude of the stagnation pressure loss ΔP_0 for the three lobed-mixer design increases slightly

with λ. It is on the order of 4.1% to 4.5%, compared to the baseline value of 3.3%. On the other hand, the stream thrust loss parameter D decreases with increasing λ. This is consistent with the numerical values for $\bar{V}_{yz}$ and the secondary-flow velocity vectors shown in Fig. 2.18, which show that the magnitude of the secondary flow motion is largest for the $\lambda=1$ case. The high value of stream thrust loss in the $\lambda=1$ case is partially due to the fact that the kinetic energy in the secondary flow motion is not useful since it does not contribute to thrust.

2.1.3 Influence of lobe geometry (varying σ)

Here the performance comparison between the baseline design and three lobed-mixer struts is presented, having values for σ as 1.0, 0.6 and 0.4. The parameters β_0 is set to 12°, while the parameter λ is set to 2. This design corresponds to a two-lobe strut with a 12° camber angle and different lobe geometry at the trailing edge. The $\sigma=1$ case corresponds to a sinusoidal lobe shape, while decreasing the value of σ to near zero yields the lobe geometry similar to the UTRC Advanced Mixer (AdM) design [19].

Figures 2.20 and 2.21 illustrate the secondary velocity vectors and the location of the wake at the outflow axial stations, respectively. It is observed that the magnitude of the secondary-flow velocity and the degree of wake distortion are very similar for these three cases. We note that as σ decreases, the distortion of the currently employed sheared H-mesh is excessive, resulting in the spurious spreading of the wake in the grid-distorted regions.

Table 3 summarizes the performance parameters. These values indicate that the parameters measuring mixing goodness are on the same order of magnitude, while the parameters measuring drag penalty increases with decreasing values of σ. It is noticed that for the $\sigma=0.4$, the numerical results of Γ_{strut} and Γ_{sec} deviate from the theoretical relation given in Eq. (6), indicating that spurious vorticity (or entropy gradient) was generated. Consequently, these results are not conclusive due to the contamination of artificial viscosity.

	baseline	$\beta_0 = 6^0$	$\beta_0 = 12^0$	$\beta_0 = 18^0$
V_{yz}	0.026	0.088	0.182	0.265
Γ_{sec}	0.000	0.193	0.409	0.632
C_1		8.8	4.4	3.0
$\frac{4\lambda\Gamma_{strut}}{\Gamma_{sec}}$	0.000	0.940	0.941	0.964
D	-0.309	-0.429	-0.768	-1.29
ΔP_o	3.31	3.72	4.44	5.70
P_{dist}	1.15	1.35	1.49	1.48

Table 2.1: Performance parameter results as a function of β_0 for $\sigma = 1$ and $\lambda = 2$ (ΔP_o and D in %)

	baseline	$\lambda = 1$	$\lambda = 2$	$\lambda = 3$
V_{yz}	0.026	0.244	0.182	0.137
Γ_{sec}	0.000	0.322	0.409	0.475
C_1		3.9	4.4	5.7
$\frac{4\lambda\Gamma_{strut}}{\Gamma_{sec}}$	0.000	0.903	0.941	0.957
D	-0.309	-1.04	-0.768	-0.624
ΔP_o	3.31	4.06	4.44	4.50
P_{dist}	1.15	1.58	1.49	1.40

Table 2.2: Performance parameter results as a function of λ for $\sigma = 1$ and $\beta_0 = 12^0$ (ΔP_o and D in %)

	baseline	$\sigma = 1$	$\sigma = 0.6$	$\sigma = 0.4$
V_{yz}	0.026	0.182	0.188	0.183
Γ_{sec}	0.000	0.409	0.416	0.409
$4\lambda\Gamma_{strut}/\Gamma_{sec}$	0.000	0.941	0.982	0.818
D	-0.309	-0.768	-0.870	-0.970
ΔP_o	3.31	4.44	5.40	6.69
P_{dist}	1.15	1.49	1.43	1.36

Table 2.3: Performance parameter results as a function of σ for $\lambda = 2$ and $\beta_0 = 12$ (ΔP_o and D in %)
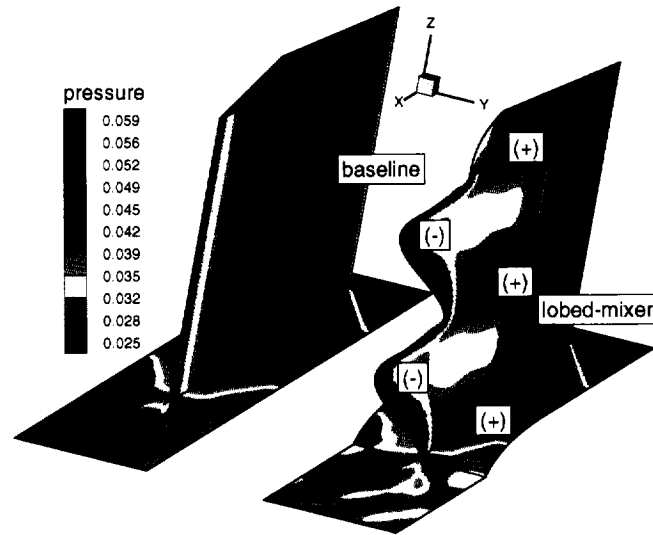
Figure 2.4: Comparison of pressure gradient along the strut.
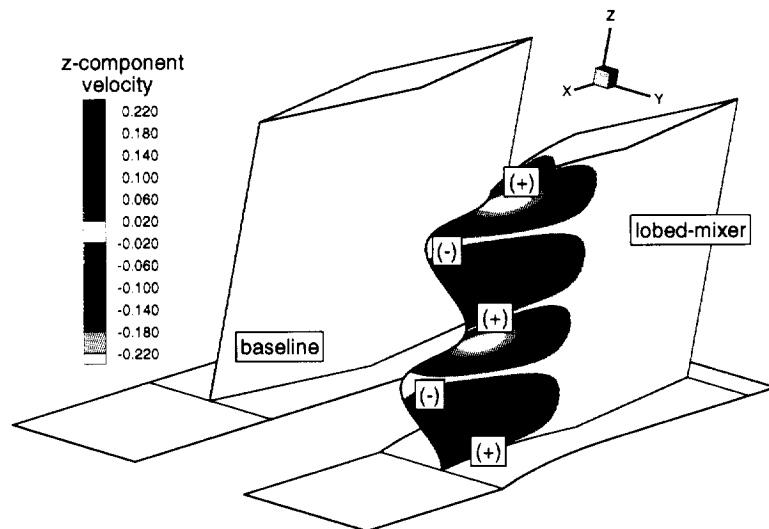
Figure 2.5: Spanwise velocity along strut surface.
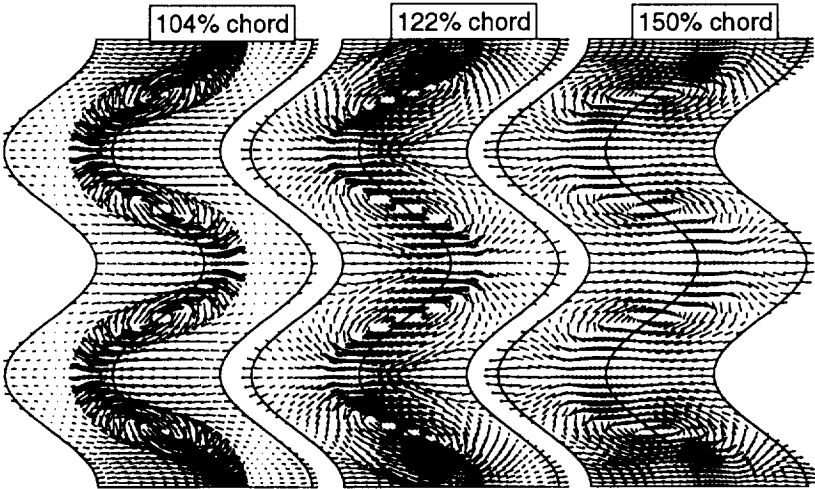
Figure 2.6: Secondary flow velocity vectors.
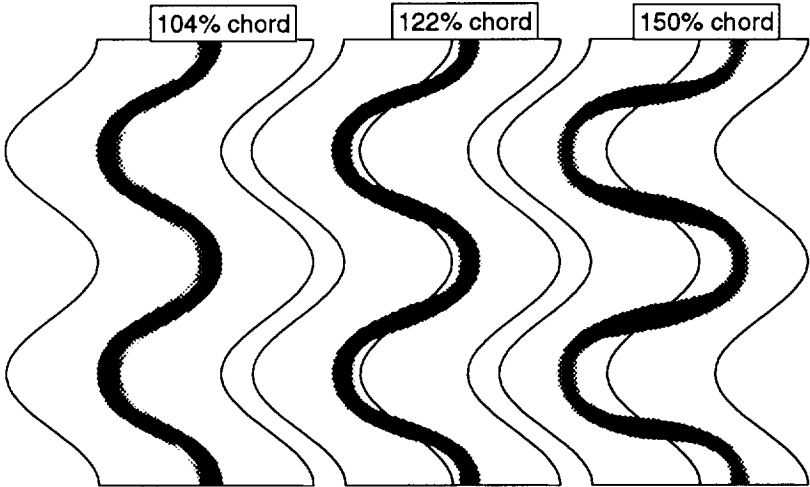
Figure 2.7: Spatial evolution of wake.
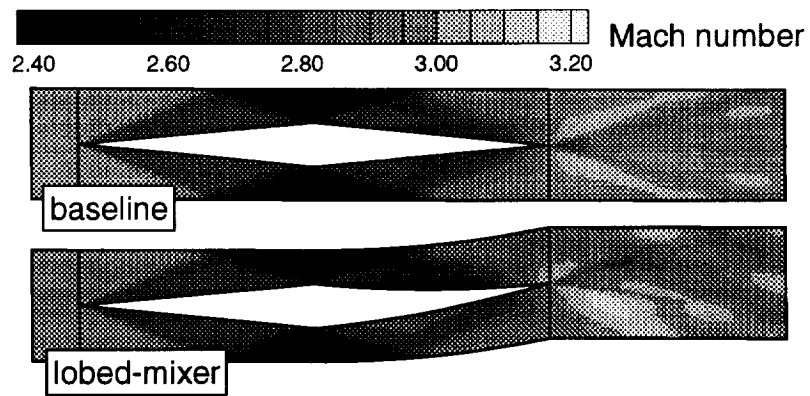
Figure 2.8: Mach number contour at midspan plane.
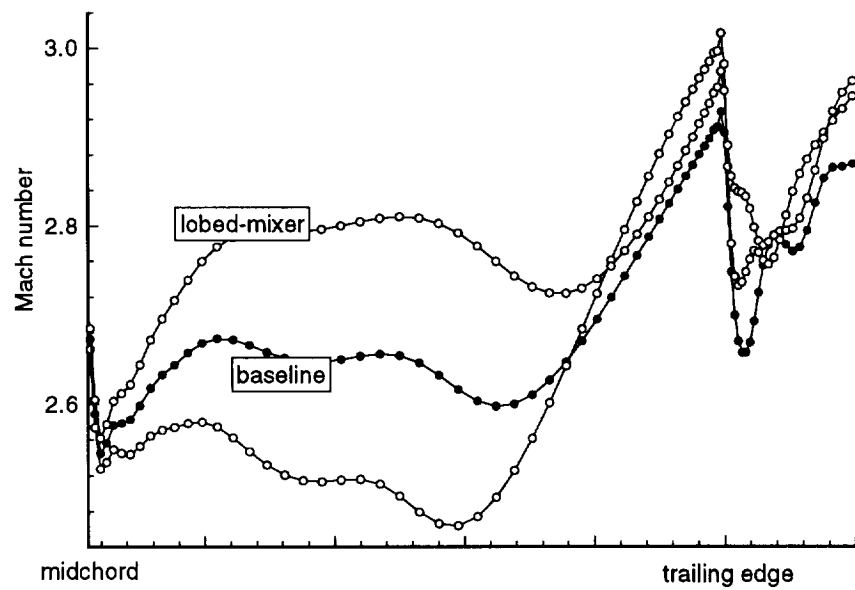
Figure 2.9: Mach number distribution along strut surface at midspan.
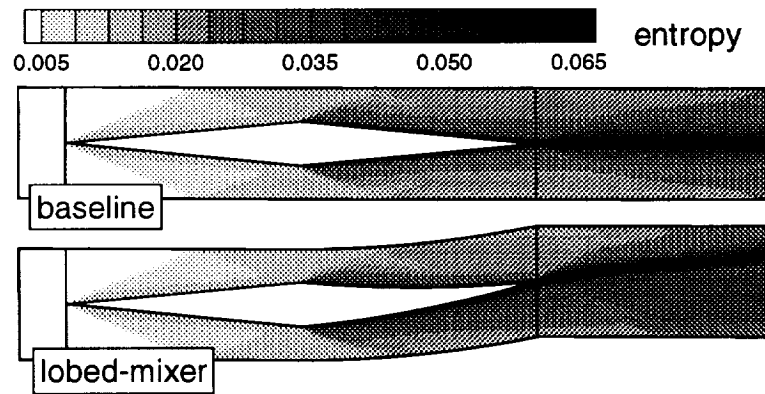
Figure 2.10: Entropy contour at midspan plane.
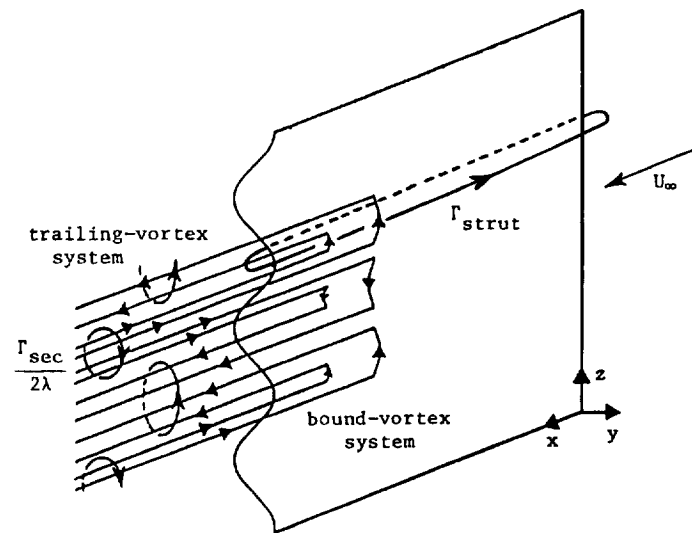
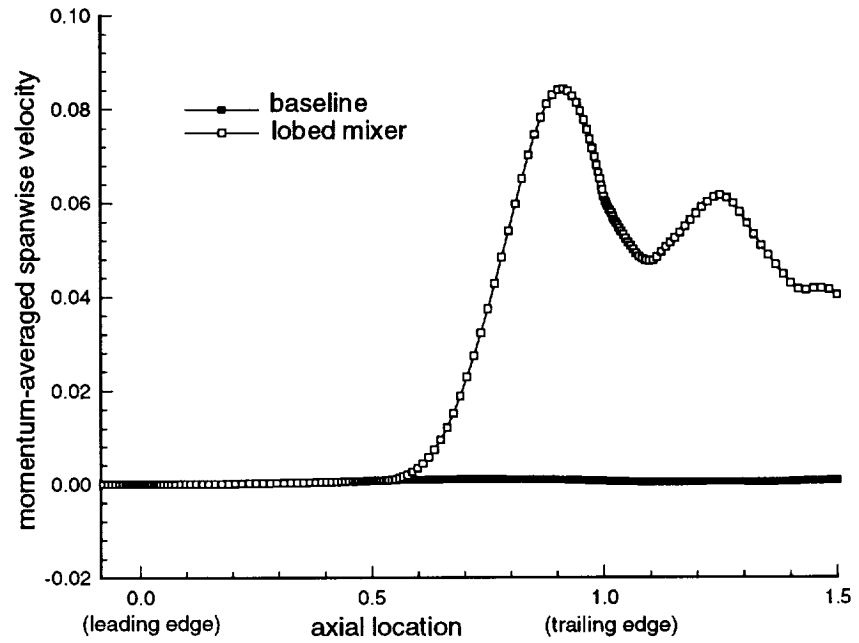Figure 2.11: Bound and trailing vortex systems representing the lobed-mixer fuel injection strut and its wake.

Figure 2.12: Momentum-averaged spanwise velocity.
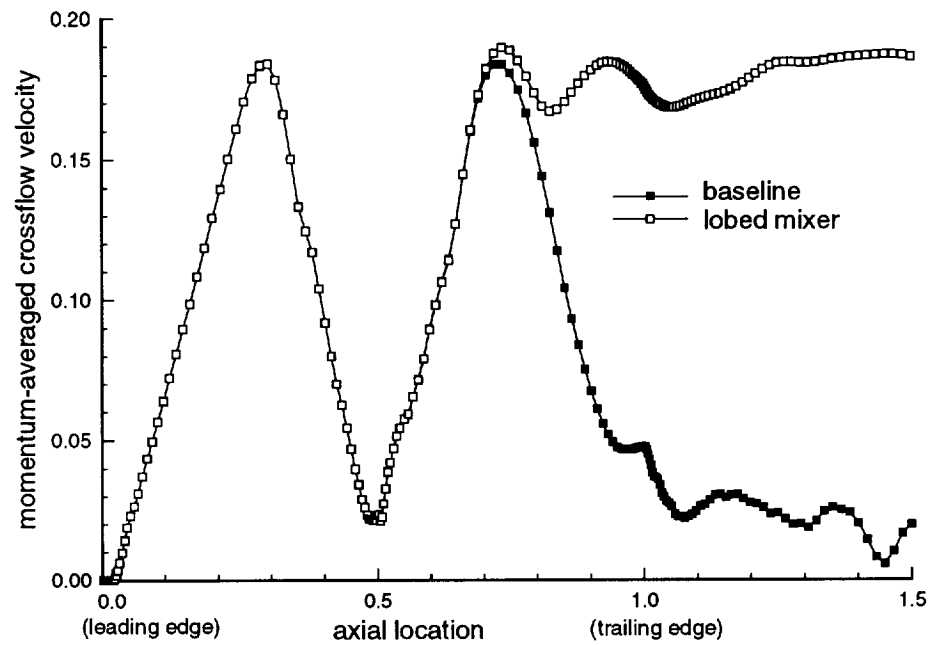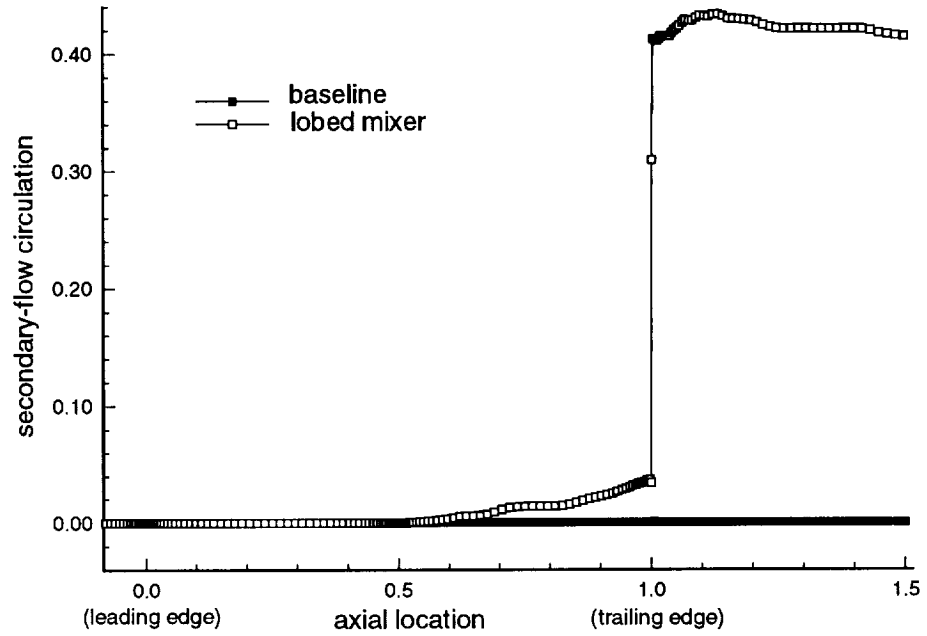

Figure 2.13: Momentum-averaged crossflow velocity.
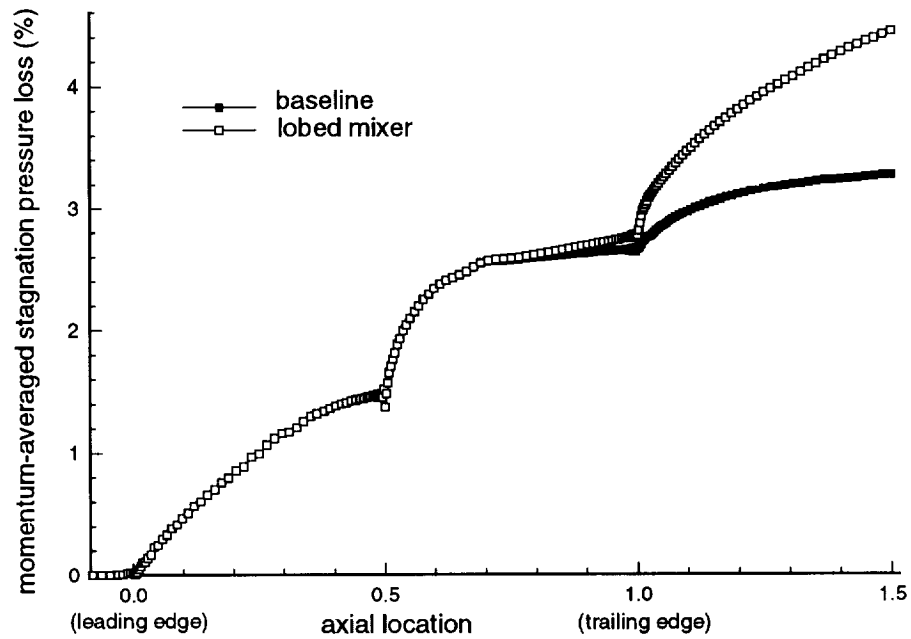
Figure 2.14: Secondary-flow circulation.
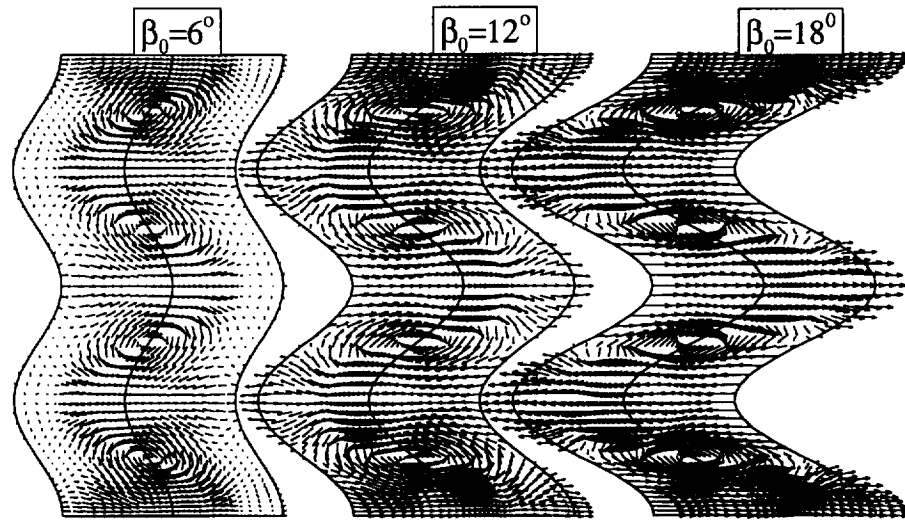

Figure 2.15: Momentum-averaged stagnation pressure loss.
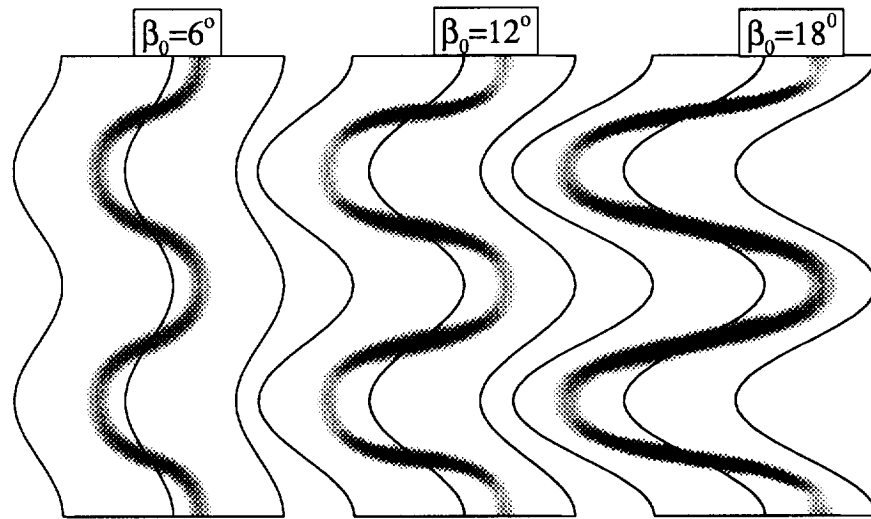
Figure 2.16: Secondary flow velocity vectors - varying β_0.
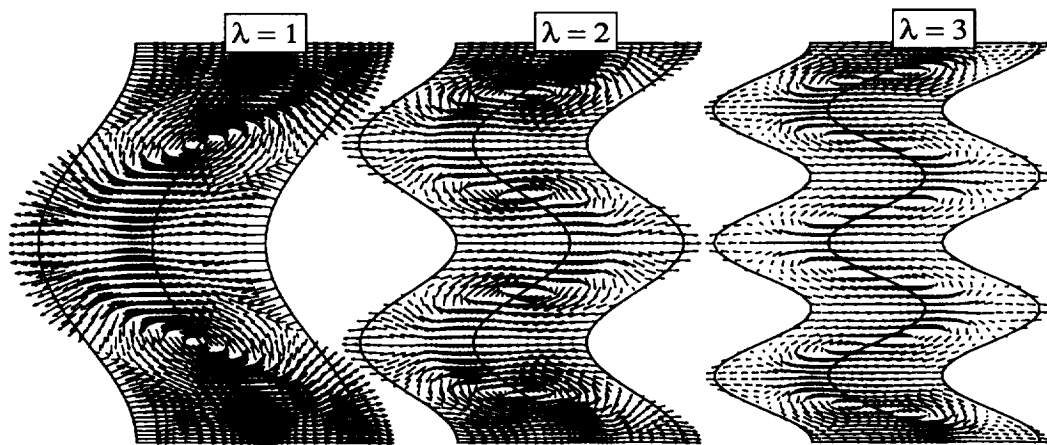

Figure 2.17: Wake distortion - β_0.
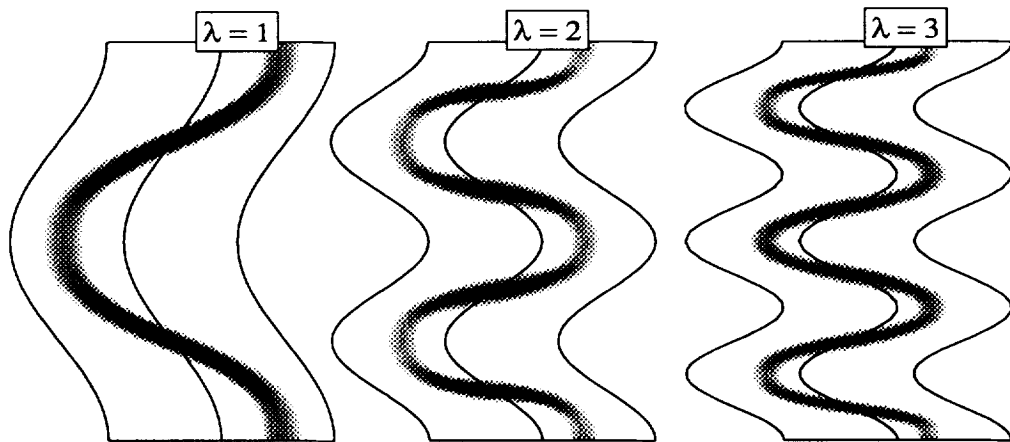
Figure 2.18: Secondary flow velocity vectors - varying λ

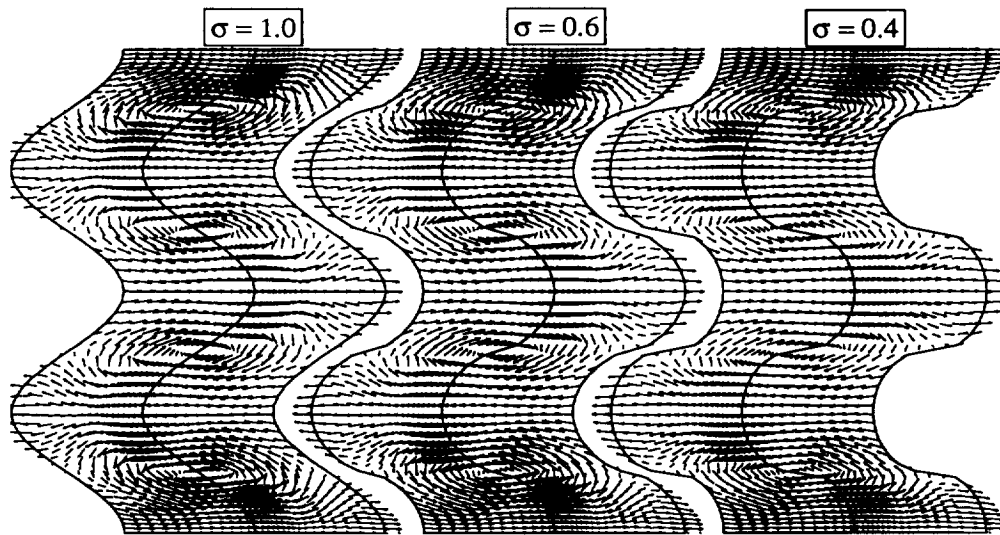Figure 2.19: Wake distortion - varying λ.

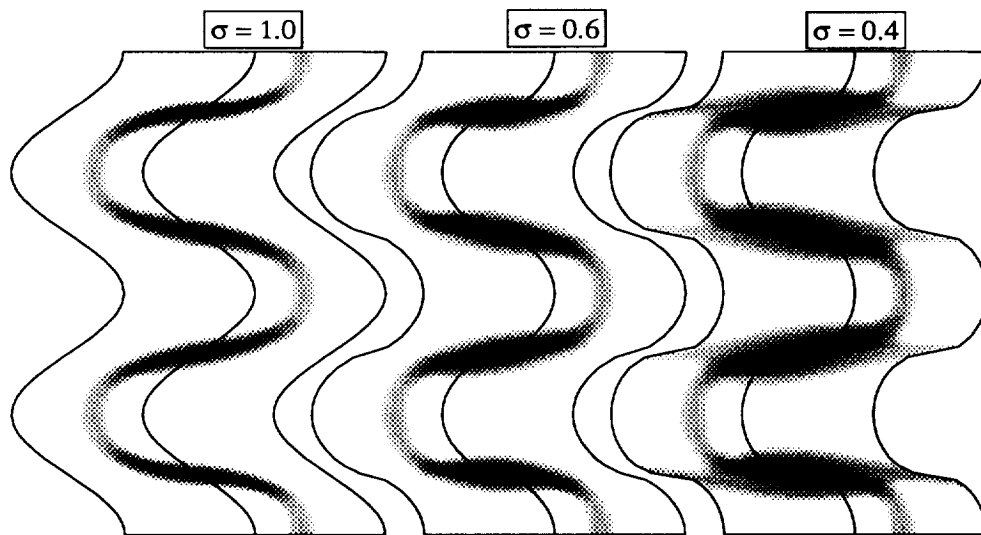Figure 2.20: Secondary flow velocity vectors - varying σ

Figure 2.21: Wake distortion - varying σ.

Chapter 3

Single Strut with Walls

The next phase of this investigation is to assess the importance of viscous effects. The NASA Langley LARCK code has been used to perform this investigation. The geometrical configuration studied is a single strut with inviscid side walls. The periodicity condition is imposed in the spanwise direction so that only 1/2-wavelength lobe needs to be considered.

The Langley Algorithm for Research in Chemical Kinetics (LARCK) Code

The LARCK code is a general purpose Reynolds-Averaged Navier-Stokes solver for reacting flows. In this code, the convective terms in the Navier-Stokes equations are discretized using upwind or central-differenced methods, while the viscous terms are central differenced. The time discretization is handled by explicit Runge-Kutta methods or implicit diagonalized approximate factorization. The implicit method allows a bigger time step or higher CFL number, and therefore faster convergence rate than the explicit method. A multigrid method is also available to further improve the convergence rate. The ability to handle complex geometries is achieved using a multiblock technique. This allows the user to decompose the computational domain into several blocks, avoiding the difficulty of generating complex geometries using the single-block approach.

All numerical schemes used for obtaining solutions to the Euler equations must contain a certain level of dissipation to (1) prevent odd-even point decoupling, (2)

maintain stability at discontinuity regions (i.e., shock waves), and (3) eliminate non-physical solutions such as expansion shocks. The dissipation may be explicitly added on top of a naturally nondissipative scheme such as pure central differencing schemes, or it may arise naturally from the spatial discretization such as in the upwind differencing schemes.

Because of the excellent capabilities in capturing strong gradients, such as the ones occurring in complex 3-D supersonic internal flows, a second order upwind scheme was the chosen and appropriate scheme for the present calculations. We choose the option of using the upwind scheme based on Roe's approximate Riemann solver and the van Leer flux limiter.

An implicit scheme was selected since these schemes allow much larger time steps, which is critical for viscous-flow calculations. However, the computational effort required in each time step can become large, especially in complex 3-D viscous calculations. To help remedy this situation a multigrid method is used. The greatest benefit of using this method is that the convergence rate remains constant, independent of the mesh spacing. An explicit scheme is not recommended to calculate the present flow field, since the time step required to attain stability can reach very small values, and consequently can be very expensive.

A total of twelve boundary conditions were imposed on the two-block grid. At the inlet, the variables were held fixed at prescribed values. At the outlet, zeroth-order extrapolation was used for the flow variables. The top and bottom boundaries were treated as periodic boundary conditions. The strut walls were treated as no-slip surfaces for the viscous simulations, and the side walls were treated as slip walls for all cases.

In the appendix, the following studies are included:

- Convergence and mesh-sensitivity studies of the LARCK code for inviscid and viscous non-reacting flows.

- Comparison of the viscous solutions using different turbulence models and Reynolds numbers for attached and separated flows.

- Consistency check of the LARCK code with a 3D Euler code developed at Syracuse University.

Scramjet Strut Model Geometry

In the preliminary investigations reported in the paper by Campuzano & Dang (1995), the following dimensions were used:

1. Aspect ratio, $H/c = 0.5$

2. Maximum thickness-to-chord ratio, $tmax/c = 0.096$

3. Spacing-to-chord ratio, $s/c = 0.24$

These dimensions are representative of the NASA-LaRC engine configurations. In this chapter, the problem was simplified by not simulating the flowfield for the entire strut, but only for a half-wavelength lobe (i.e. periodicity condition in the z-direction - see Fig. 1.1) with a camber angle at the trailing edge of twelve degrees, and symmetric boundary conditions were imposed in the y-direction. Slip-wall boundary conditions were employed in the z-direction. The new dimensions for this case are:

1. Aspect ratio, $H/c = 0.25$

2. Maximum thickness-to-chord ratio, $tmax/c = 0.1$

3. For the single strut case, $s/c = 0.4$ (s is the spacing between the side walls)

Viscous Turbulent-Flow Calculation

The molecular viscosity was calculated using the Sutherland law. The laminar and turbulent Prandtl numbers chosen were 0.72 and 0.9 respectively. The two-equation model of Menter was used for the calculations along with the compressibility correction of Sarkar and a Reynolds number of one million based on the strut chord. A multigrid scheme was also used with a V cycle. Implicit time integration was applied using CFL numbers up to 4.

To meet viscous sublayer requirements, grid clustering was applied along all no-slip surfaces (i.e. along the strut surface). The formula used to calculate the boundary layer thickness was the common incompressible turbulent flow formula found in common classic introductory fluid mechanics books, namely:

$$\frac{\delta}{c} = \frac{0.37}{Re^{\frac{1}{5}}} \tag{3.11}$$

The Reynolds number is one million, so the boundary layer thickness at the trailing edge is $\delta = 0.02335$ for a chord of unit length. To find the minimum distance to the wall, the following criteria was selected (based on the u^+ - y^+ graph):

$$\frac{5}{500} = 0.01 \qquad\qquad \Delta y_{min} = 0.01\delta = 0.0002335 \tag{3.12}$$

The first grid point from the wall is at $y = 0.0001$, the second is at $y = 0.00023$, the third, at about $y = 0.0005$, the fourth at $y = 0.00095$, the fifth at $y = 0.0018$.

For the buffer zone:

$$y^+ = 10 \qquad\qquad \frac{10}{500} = 0.02 \qquad\qquad \Delta y_{min} = 0.02\delta = 0.000467 \tag{3.13}$$

$$y^+ = 30 \qquad\qquad \frac{30}{500} = 0.06 \qquad\qquad \Delta y_{min} = 0.06\delta = 0.0014 \tag{3.14}$$

So, about two points are inside the viscous sublayer zone, and about two in the buffer zone. The remaining are distributed along the wall to strut plane.

3.1 Inviscid and Viscous Results without Flow Separation for the Lobed-Mixer Strut

In this section a comparative study of the influence of viscosity on streamwise vorticity generation, convection, and dissipation is carried out. The inlet Mach number is taken to be 2. Figure 3.22 shows the pressure contour along the J=1 plane. At this location, the strut has the maximum camber and consequently the maximum penetration and

circulation. The figure illustrates that the overall flowfield between the inviscid and the viscous solutions are very similar since viscous effects are isolated to thin boundary layers along the strut surfaces.

Figures 3.23 and 3.24 shows the axial distribution of the momentum-averaged spanwise velocity and momentum-averaged crossflow-velocity. From the inlet to the 50% chord location, the inviscid and viscous cases have zero spanwise velocity. In this region the two flowfields are nearly two-dimensional, and the crossflow velocity is composed primarily of the transverse z-component velocity acquired by the flow as it crosses the oblique shock system. From these two figures, we note that the z-component velocity is higher for the viscous case than for the inviscid case. This difference is due to the stronger oblique shock at the leading edge for the viscous case due to the presence of a boundary layer which increases the effective wedge angle at the leading edge. After the 50% chord location, both cases show a similar behavior in spanwise velocity magnitude, with the viscous case showing a slightly less magnitude. The appearance of the spanwise velocity indicates that the flow is now three-dimensional (Fig. 3.23), with viscous effects reducing the magnitude of the spanwise velocity slightly.

The crossflow velocity magnitude is about 9% and 8.2% of the freestream velocity at 50% chord downstream, for the inviscid and viscous cases, respectively. The higher magnitude for the inviscid case is attributed to the higher loading along the strut surface as can be seen from figure 3.25. This higher loading will result in higher lift or circulation. The cross-velocity vectors at the outlet are shown in figure 3.26. It can be seen that the strength of the vortex is similar for both cases.

Figure 3.27 shows the axial distributions of the secondary-flow circulation from the inlet to the outlet. The circulation for the forward half of the strut is nearly zero for both cases, thus zero lift or no secondary flows are present. After the midchord, the circulation increases up to the trailing edge due to the spanwise pressure gradient generated by the lobe strut. We note that the definition of secondary-flow circulation is slightly different from the definition given in Eq. (2.4). Here, the circulation in the strut region is taken along a path that includes the strut. Hence it includes includes

the bound vortex system. This explains why the circulation is non-zero in the strut region.

Two important things can be noticed here. First, as a result of a slightly higher strut loading for the inviscid case, it is expected that the secondary flow magnitude will be higher for the inviscid case. This is confirmed by the figures presented so far (i.e. Figs. 3.23 and 3.27). Second, viscosity plays little role in the generation of the streamwise vorticity, it is purely an inviscid phenomena. In the case of non-separated flow, viscosity introduces blockage into the flowpath, causing a reduction in the strut loading, and therefore slightly affects the strength of the secondary flow. In summary, this section demonstrates that viscous effects are not important when flow separation is absent.

3.2   Inviscid and Viscous Results with Flow Separation for the Lobed-Mixer Strut

In this section, results are presented for an inflow Mach number of 3. In this case, flow separation occurs along the strut suction surface, as can be seen in figure 3.28. The flow separates at the trailing edge portion of the strut as a result of the shock impingement on the strut. In general the inviscid and viscous solutions are similar on the pressure side of the strut, while the solutions on the suction side are quite different (Figs. 3.29 and 3.30). In particular, the strut trailing edge shock is stronger for the inviscid case. On the other hand, in the viscous case, the shock wave is weakened considerably due to the strong separation zone occurring on the strut suction surface, as can be seen from figure 3.29.

Figure 3.30 shows the comparison of the pressure distribution along the strut surfaces at the maximum camber station (J=1). Note that the viscous and inviscid solutions predict nearly the same pressure distribution along the pressure surface where the flow is attached, while the solutions are very different along the suction surface where the flow separates. Figure 3.30 shows that the presence of a large separated flow region in the viscous-flow case dramatically reduces the loading along the

strut. Consequently, it is expected that the viscous flow case produces less secondary flow than the inviscid case, as will be discussed shortly. Figure 3.31 shows the entropy at the outlet. The entropy level is much higher in the viscous case than the inviscid case, indicating that losses associated with shock waves are much smaller than viscous losses. The high-loss regions at the top and bottom boundaries correspond to the separated-flow regions. The high-loss regions near the mid-section are associated with the wake behind the attached-flow section of the strut (and some numerical entropy generated by the vortex sheet). Figure 3.32 shows comparison of the secondary flow velocity vectors for the viscous and inviscid cases. The two secondary flow patterns are relatively different when compared the the Mach-2 freestream case (see Fig. 3.26).

Figures 3.33 and 3.34 show the axial distribution of the momentum-averaged spanwise velocity and momentum-averaged crossflow-velocity. From the inlet to the 50% chord location, the inviscid and viscous cases have zero spanwise velocity. In this region the two flowfields are nearly two-dimensional, and the crossflow velocity is composed primarily of the transverse z-component velocity acquired by the flow as it crosses the oblique shock system. Again, the viscous solution indicates that the leading-edge shock is stronger for the viscous case than for the inviscid case due to the presence of the boundary layer which increases the effective wedge angle at the leading edge. After the 50% chord location, both cases show a similar behavior in spanwise velocity magnitude, with the viscous case showing considerably less magnitude. The appearance of the spanwise velocity indicates that the flow is three-dimensional.

The crossflow velocity magnitude is about 14% and 12% of the freestream velocity at the outlet (50% chord downstream) for the inviscid and viscous cases, respectively. It is also noticed that the z-component (transverse) velocity is higher for the viscous case from the leading edge of the strut to the mid chord. This is due to the leading edge shock angle been higher for the viscous case, as the incoming flow sees the boundary layer formed along the strut surface. The spike present at the strut midchord in the crossflow velocity (Fig. 3.34) for the inviscid case appears to be attributed to numerical errors. The spike is not present in the momentum-averaged spanwise velocity plot shown in Fig. 3.33. It is present in the momentum-averaged

transverse velocity plot shown in Fig. 3.37. This indicates that the error is associated with the expansion fan at the mid chord location, and the error is probably dispersive in nature.

Figure 3.35 shows the axial distributions of the secondary-flow circulation from the inlet to the outlet. The secondary-flow circulation for the forward half of the strut is nearly zero for both cases. After the midchord, the circulation increases gradually up to the trailing edge. The secondary-flow circulation is much larger for the inviscid case than for the viscous case, as expected. In the viscous case, the flow separation region reduces the lift and accounts for the reduction in secondary flow. The drop in secondary-flow circulation behind the strut for the inviscid case is explained in the next section.

In summary, this section demonstrates that viscous effects are extremely important when flow separation occurs. Flow separation can reduce the lift of the strut and hence a reduction in secondary flow.

3.3   Effect of Mach Number for Inviscid Flow

The effects of Mach number on the strength of the secondary flow are examined here by comparing the Mach-2 and Mach-3 cases presented in the previous sections. To carry out this task, we examine the inviscid-flow solutions so that the effects of flow separation on the generation of secondary flow are isolated. Comparisons of the spanwise (Fig. 3.36), transverse (Fig. 3.37), and crossflow (Fig. 3.38) velocities behind the strut show that the strength of the secondary flow for the Mach-3 case is much higher than for the Mach-2 case. Inspection of the strut pressure loading shows that the lift produced by the Mach-3 case is indeed twice larger than the Mach-2 case (Fig. 3.39), which correlates with the axial distribution of secondary-flow circulation shown in Fig. 3.40.

In Fig. 3.40, it is interesting to note that there is a drop in secondary-flow circulation for the Mach-3 case behind the strut, while this quantity is conserved for the Mach-2 case. Based on the theory of inviscid flow, we expect the circulation of the trailing vortex system to be conserved behind the strut! Figures 3.41 and 3.42

show the axial vorticity field at 10%- and 25%-chord behind the strut trailing edge. The figure shows that the axial vorticity is minimum at the maximum-lift section (i.e. bottom or J=1 station) and reaches the maximum at the zero-lift section (i.e. midspan or J=21 station). We then track the streamlines leaving the strut trailing edge at 3 spanwise stations (Figs. 3.43-3.45). These streamlines are representative of the trailing-vortex system. These figures clearly show that at the J=11 station (Fig. 3.44) where the axial vorticity is non-zero, the trailing-edge streamline shifts significantly in the z direction. Since the secondary-flow circulation is defined as

$$\Gamma_{sec}(x) \equiv \int\int |\vec{\Omega}| \cdot \hat{e}_x(dydz) = \int\int |\Omega_s|cos\theta(dydz) \qquad (3.15)$$

we conclude that the magnitude of the secondary-flow circulation is reduced by an amount proportional to $cos(\theta)$, where θ is the angle formed between the x-axis and the trailing-edge streamline. Figures 3.43-3.45 clearly show that the angle θ is invariant for the Mach-2 case, while it increases with streamwise distance from 0° to around 30° for the Mach-3 case (Fig. 3.43 and 3.44). Hence, the secondary-flow circulation is conserved behind the strut for the Mach-2 case, while it decreases for the Mach-3 case. A reduction from 0.28 to 0.22 for the Mach-3 case as shown in Fig. 3.40 suggests that θ should change from 0° to 35°, which is a little larger than what is shown in Figs. 3.43 and 3.44. This can be explained by the fact that the streamline distortion in the y-direction can also contribute to this reduction.

3.4 Baseline vs Lobed-Mixer Strut

In this section, we compare the baseline and lobed-mixer viscous solutions. The comparisons are made for the Mach-2 case where flow separation is absent.

Figure 3.46 shows the pressure contour at the J=1 station where the camber (or circulation) is highest for the lobe-mixer geometry. Figure 3.47 shows the pressure along the strut surface at J=1. It can be observed that the baseline case has zero lift and therefore no generation of secondary flows, and the lobed mixer case is characterized by the generation of lift and therefore secondary flow circulation is generated.

Figure 3.48 shows the cross-flow velocity vectors at the outlet axial plane. It is clearly seen that the flow is two-dimensional in the baseline case, whereas the lobed-mixer case produces streamwise vorticity concentrated at the zero-lift spanwise station. Figure 3.49 shows the axial distributions of the momentum-averaged spanwise velocity. From the inlet to the 50% chord location, the baseline and lobed-mixer cases have zero spanwise velocity. In this region the two flowfields are nearly two-dimensional. After the 50% chord location, the spanwise velocity increases significantly for the lobed-mixer case while the spanwise velocity for the baseline case remains near zero. This increase in spanwise velocity for the lobed-mixer case indicates that the flow is three-dimensional.

Figure 3.50 shows the axial distribution of the secondary-flow circulation. The figure shows that the baseline case has zero axial vorticity while the circulation for the lobed-mixer case increases due to the strong streamwise vorticity generation. Figure 3.51 shows the loss in total pressure for the two cases. This figure shows that the loss for both cases is nearly the same up to the trailing edge, indicating that the additional shock loss due to strut cambering is insignificant! In the region behind the strut, the stagnation pressure loss is larger for the lobed-mixer than the baseline geometry (about 17% percent higher at the outflow boundary). This increase in loss is due to the stronger shock near the trailing edge for the lobed-mixer case, and to the viscous dissipation of the secondary flow (or mixing loss).

	baseline	lobed-mixer
$\overline{V_y}$	0.00	0.058
Γ_{sec}	0.000	0.139
D	-0.618	-1.006
ΔP_o	2.99	3.43

Table 3.4: Performance parameter results (ΔP_o and D in %)

Table 3.4 summarizes the performance parameters obtained from the numerical solutions. It clearly shows that the lobed-mixer produces significant secondary flows

at 50% chord downstream, more than an order of magnitude when compared to the baseline case. In terms of drag penalty, the stream thrust loss in the baseline case is 0.62%, while the stream thrust loss in the lobed-mixer is 1.0%. Finally, the change in total pressure is 3.0% for the baseline and 3.43% for the lobed-mixer case.

Comparison of Euler/Navier-Stokes

Mesh 160x40x80   J=1
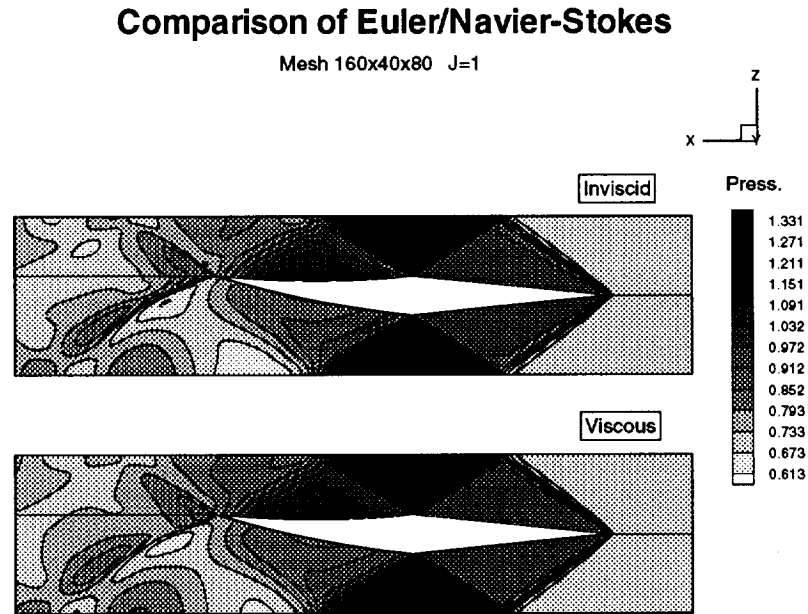
Figure 3.22: Pressure contour at the J=1 plane.
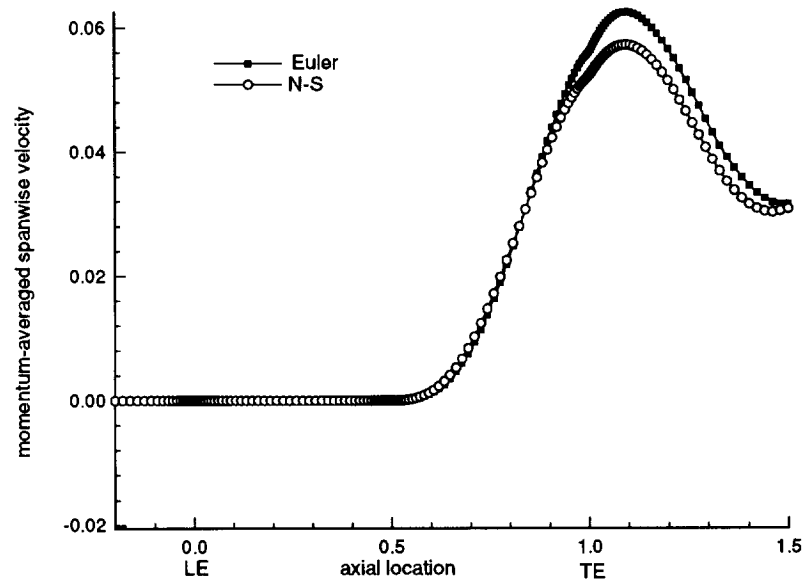
Figure 3.23: Comparison of spanwise velocity for inviscid and viscous cases.
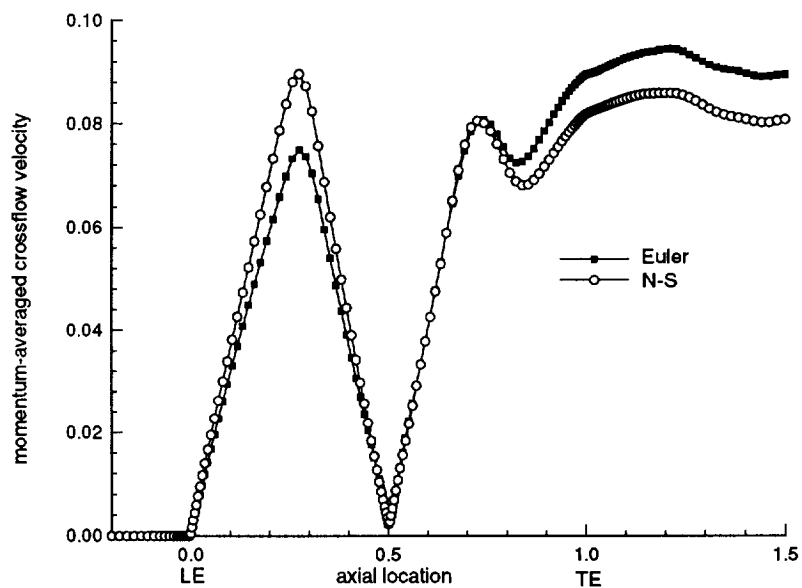
Figure 3.24: Comparison of momentum-averaged crossflow velocity for inviscid and viscous cases.
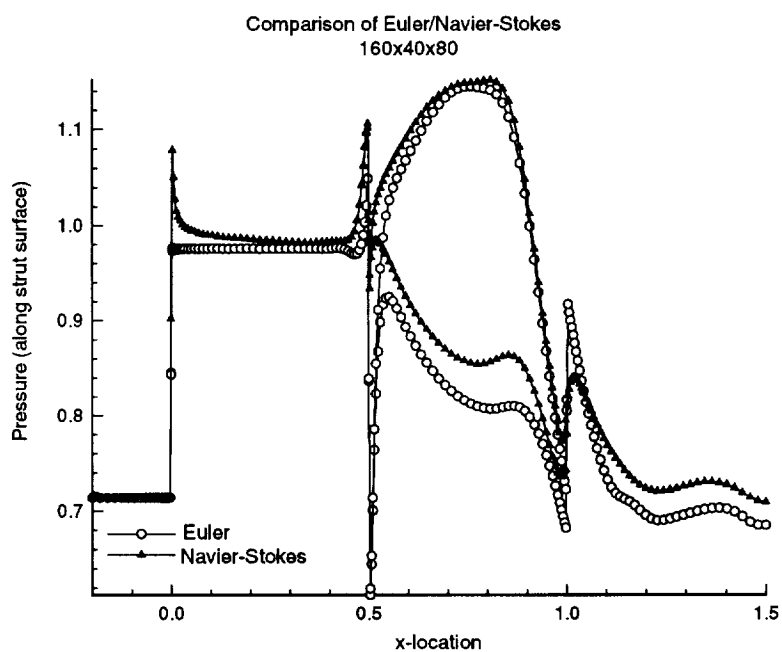
Figure 3.25: Pressure along strut surface at J=1.

Comparison of Euler/Navier-Stokes

Cross-velocity vectors at I=161 (at outlet)

160x40x80
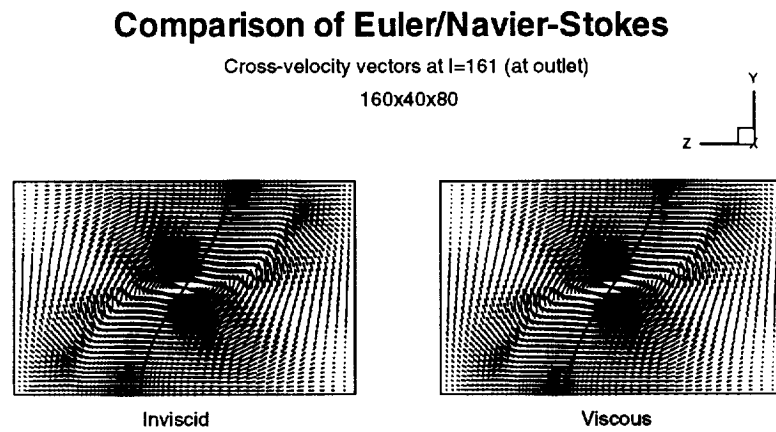
Inviscid   Viscous

Figure 3.26: Cross velocity vectors at outlet.
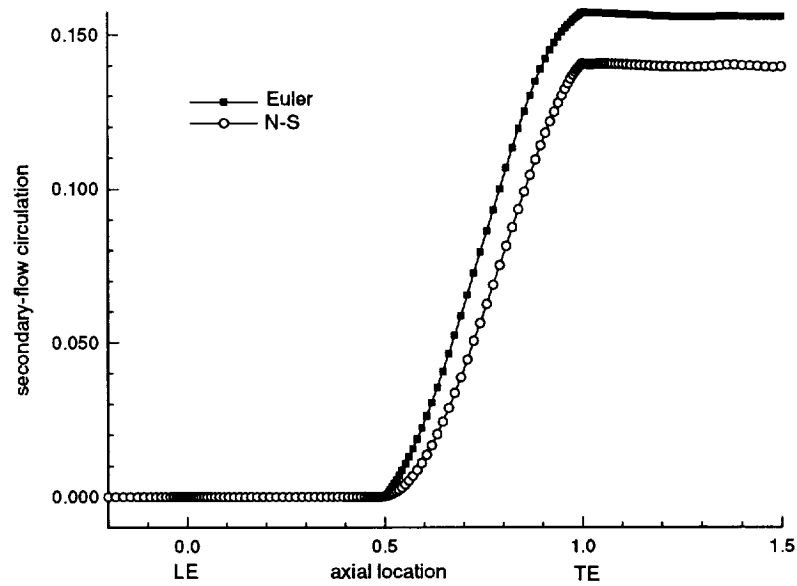
Figure 3.27: Comparison of secondary circulation for inviscid and viscous cases.

Mesh sensitivity study for Viscous solution

Separation region close-up for 160x40x80
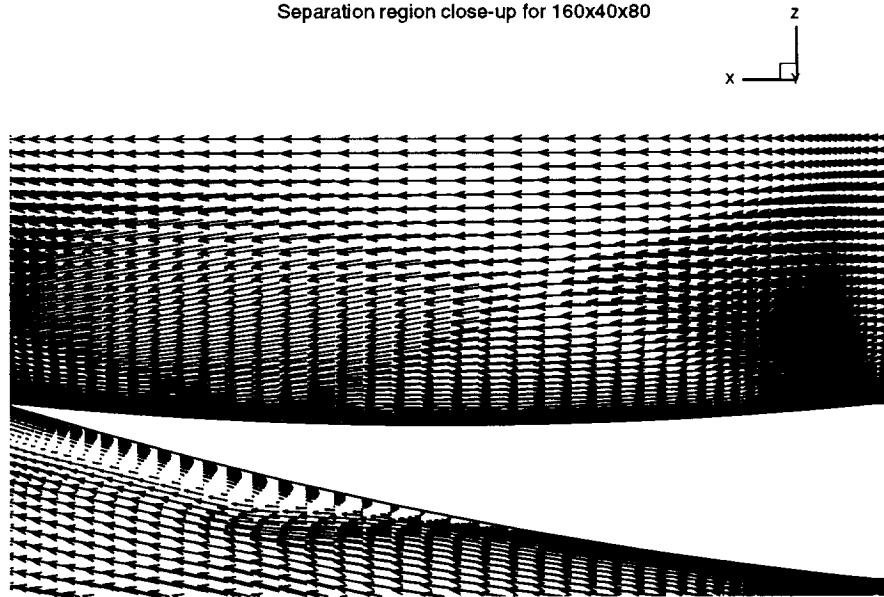
Figure 3.28: Separation region close-up.

Comparison of Euler/Navier-Stokes

Mesh 160x40x80 J=1
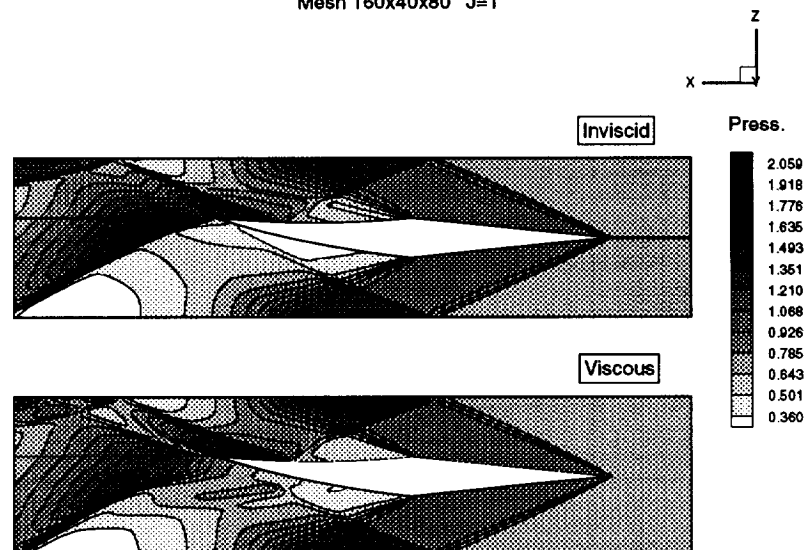
Figure 3.29: Comparison of pressure contour at J=1.
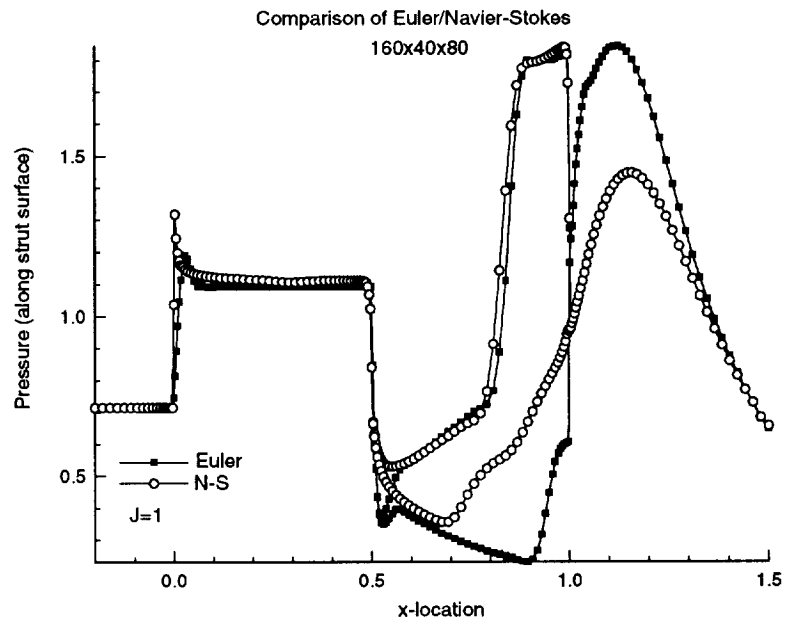
Figure 3.30: Comparison of pressure along strut surface at J=1.
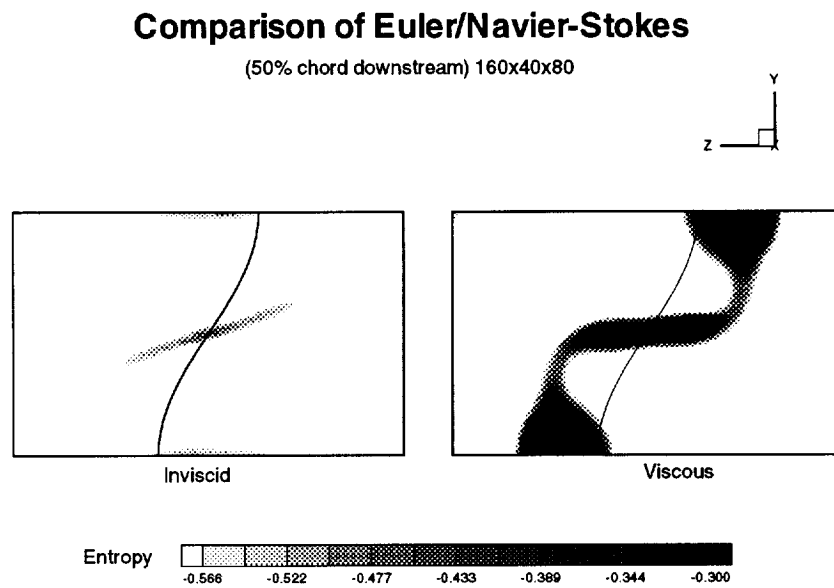
Figure 3.31: Comparison of entropy at outlet.

Comparison of Euler/Navier-Stokes

Cross-velocity vectors at I=161 (at outlet)

160x40x80

Inviscid

Viscous
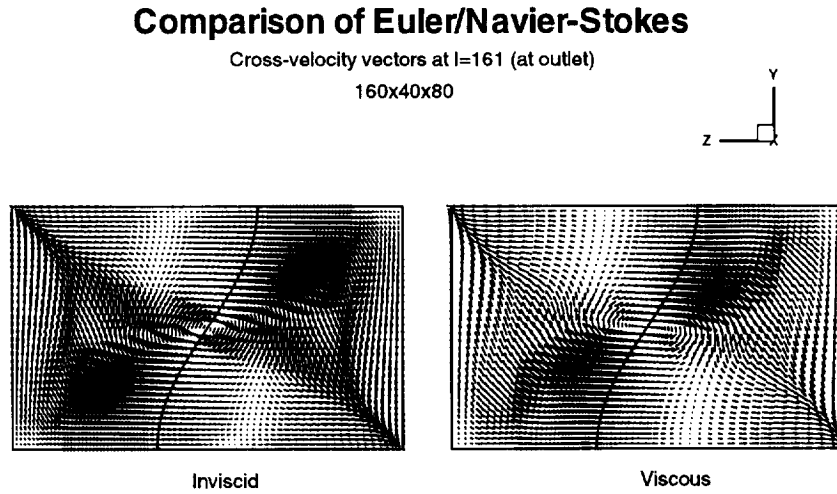
Figure 3.32: Comparison of cross-velocity vectors at outlet.
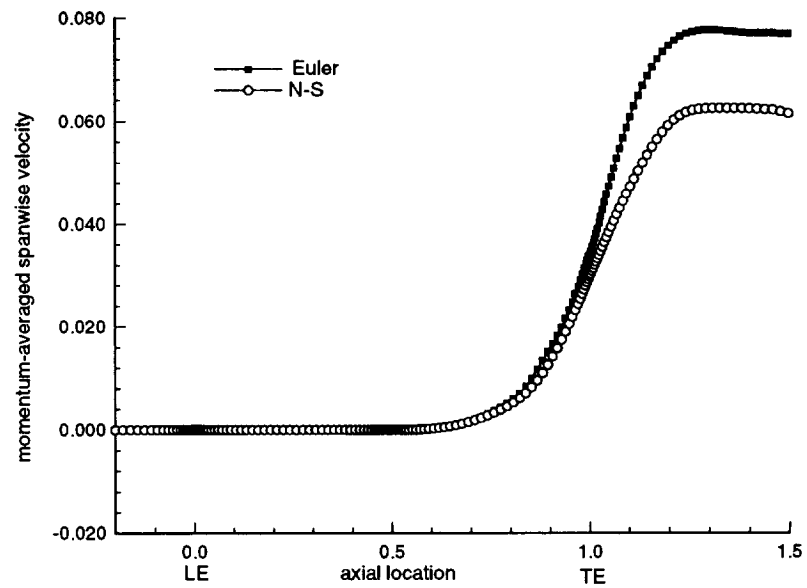
Figure 3.33: Comparison of momentum-averaged spanwise velocity.
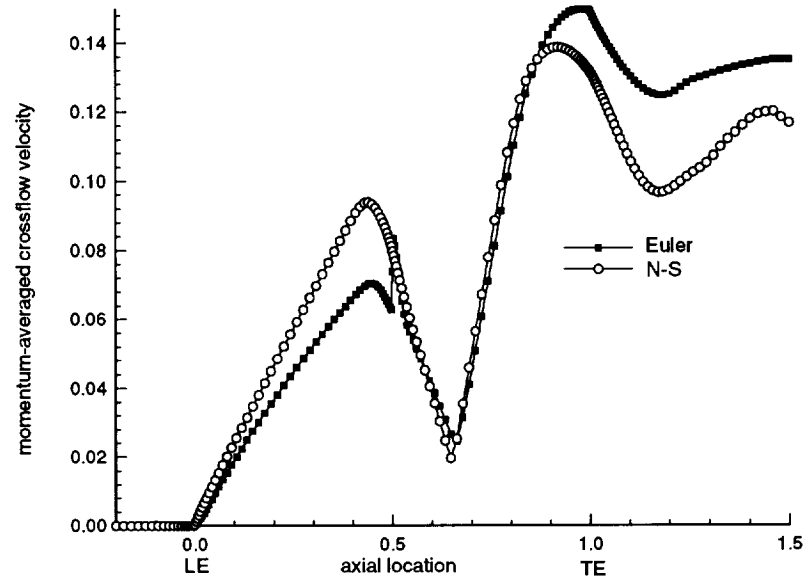
Figure 3.34: Comparison of momentum-averaged crossflow velocity.
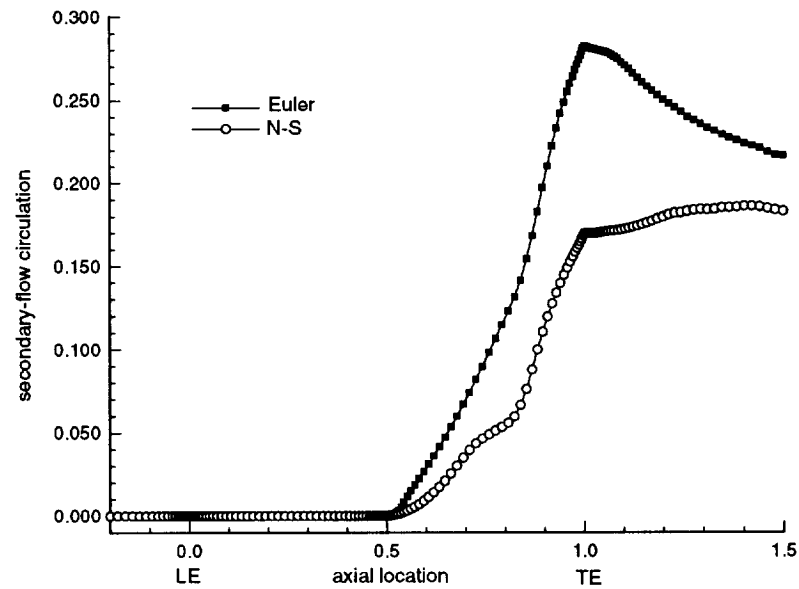
Figure 3.35: Comparison of secondary circulation for inviscid and viscous cases.
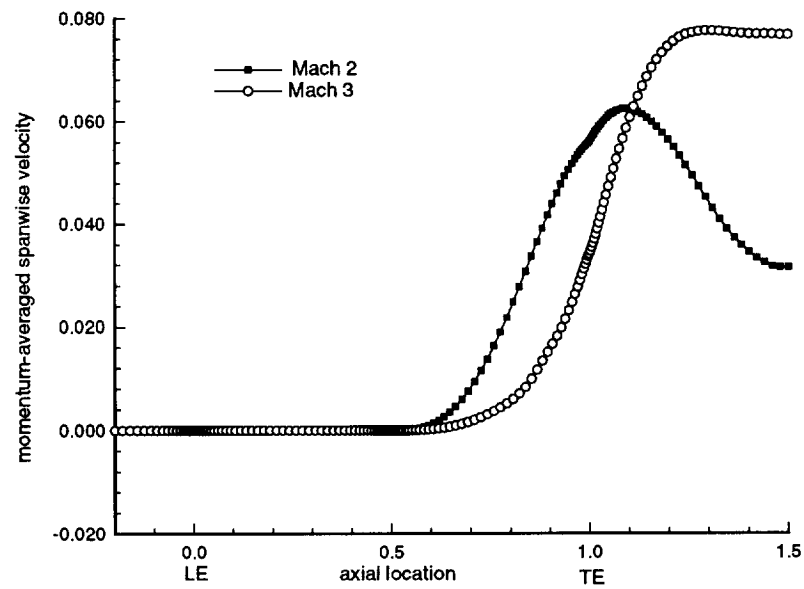
Figure 3.36: Comparison of momemtum averaged spanwise velocity.
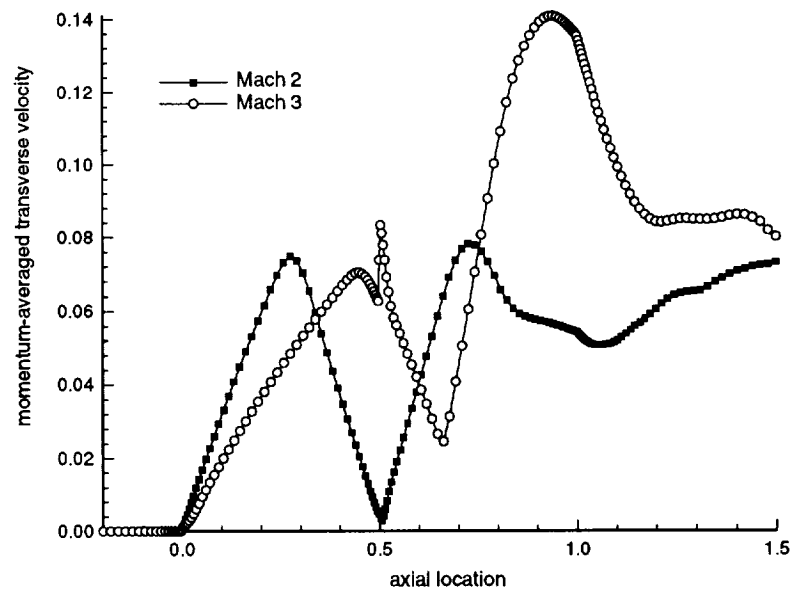
Figure 3.37: Comparison of momemtum averaged transverse velocity.
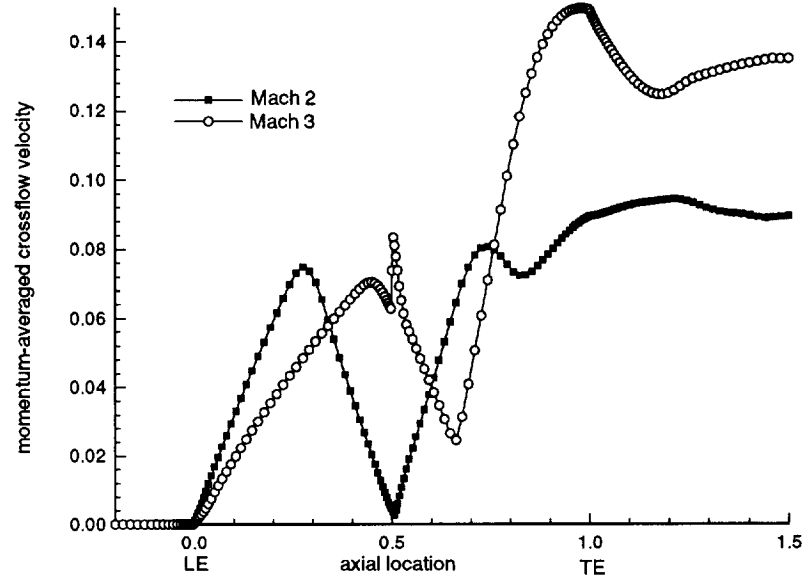
Figure 3.38: Comparison of momemtum averaged crossflow velocity.
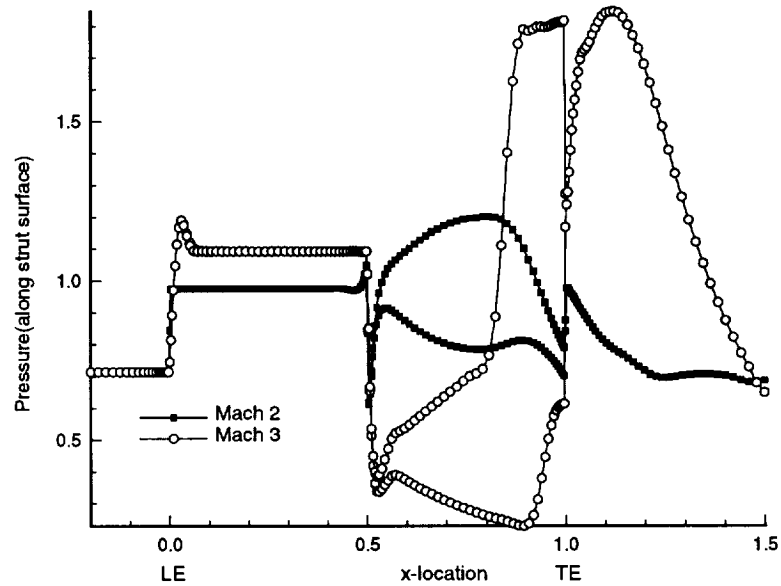
Figure 3.39: Comparison of pressure along strut surface at J=1.
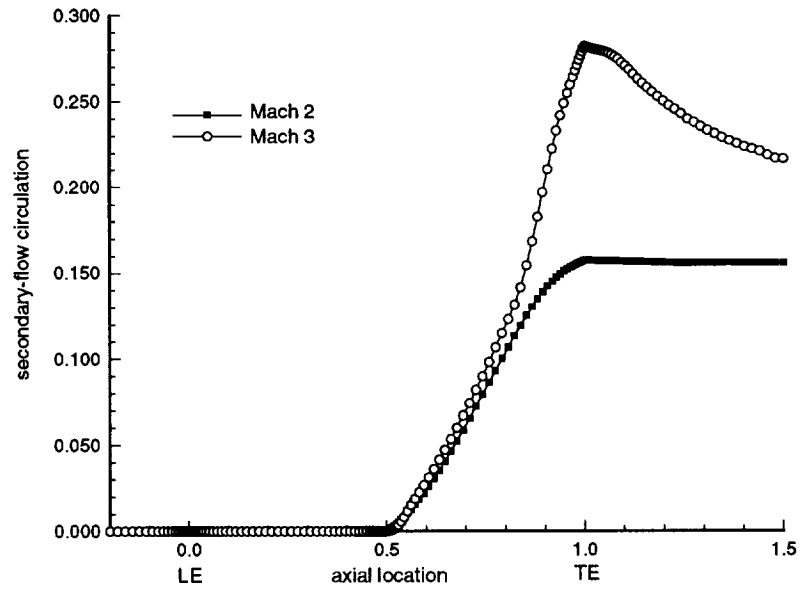
Figure 3.40: Comparison of secondary-flow circulation.
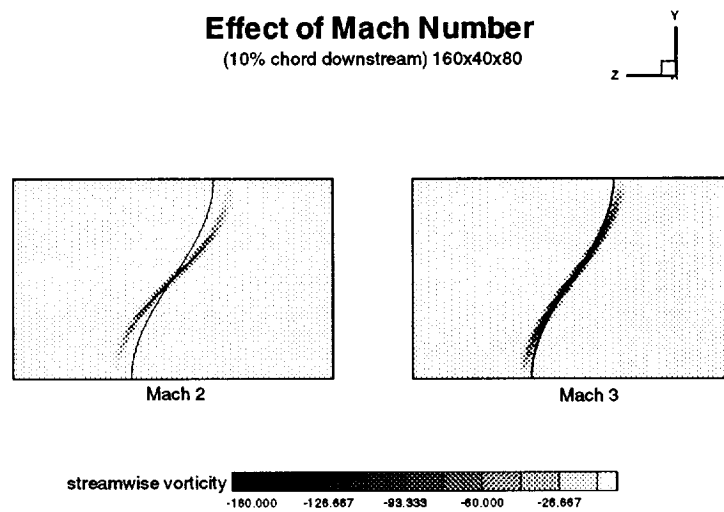
Figure 3.41: Comparison of axial vorticity contour at 10%-chord behind strut traili ng edge.

Effect of Mach Number
(25% chord downstream) 160x40x80

Mach 2

Mach 3

streamwise vorticity
-160.000 -126.667 -93.333 -60.000 -26.667
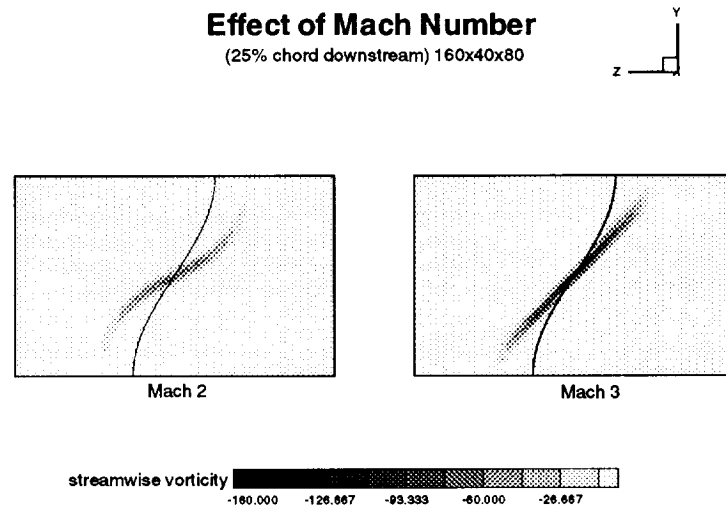
Figure 3.42: Comparison of axial vorticity contour at 25%-chord behind strut traili ng edge.

Streamwise Comparison
J=1

Mach 2

Mach 3
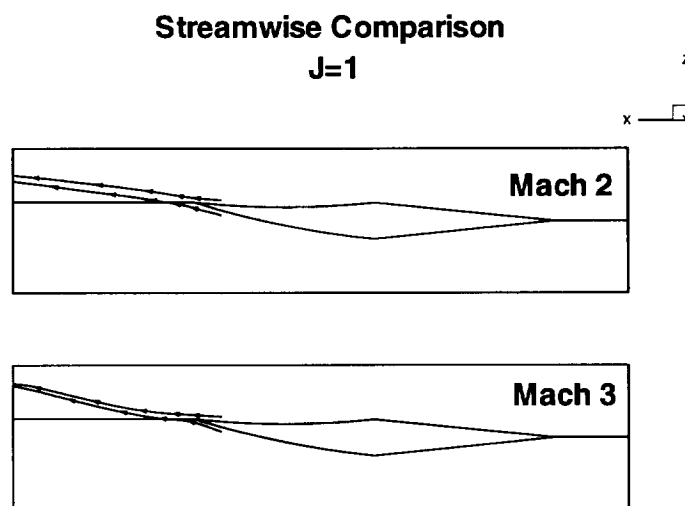
Figure 3.43: Comparison of streamlines at J=1.

Streamlines Comparison
J=11

Mach 2

Mach 3
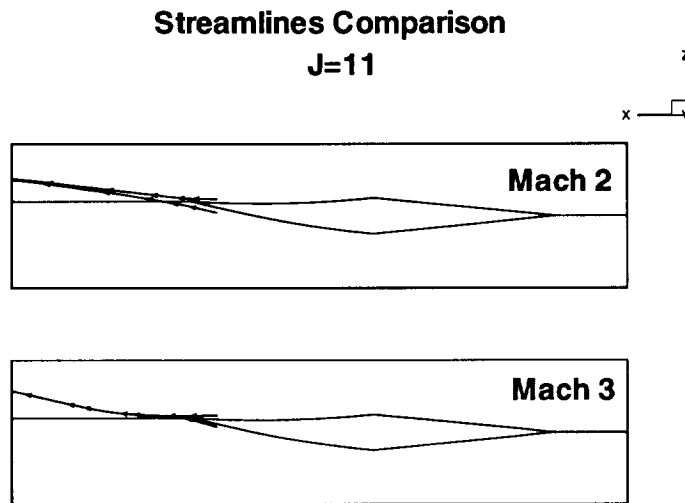
Figure 3.44: Comparison of streamlines at J=11.

Streamlines Comparison
J=21

Mach 2

Mach 3
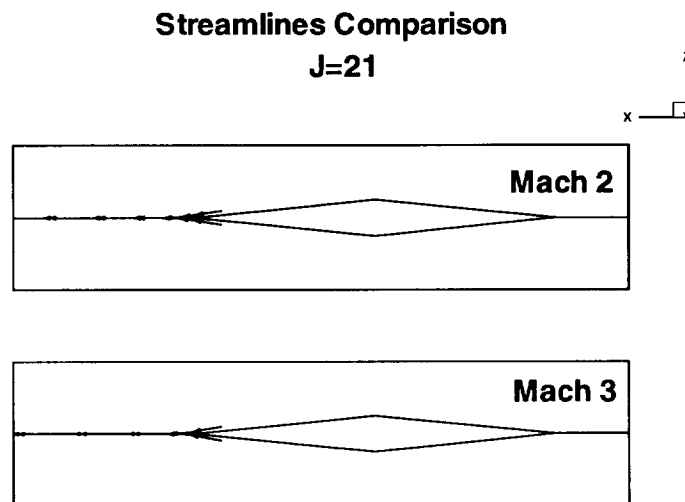
Figure 3.45: Comparison of streamlines at J=21.

Comparison of Baseline/Lobed-Mixer

Mesh 160x40x80 J=1
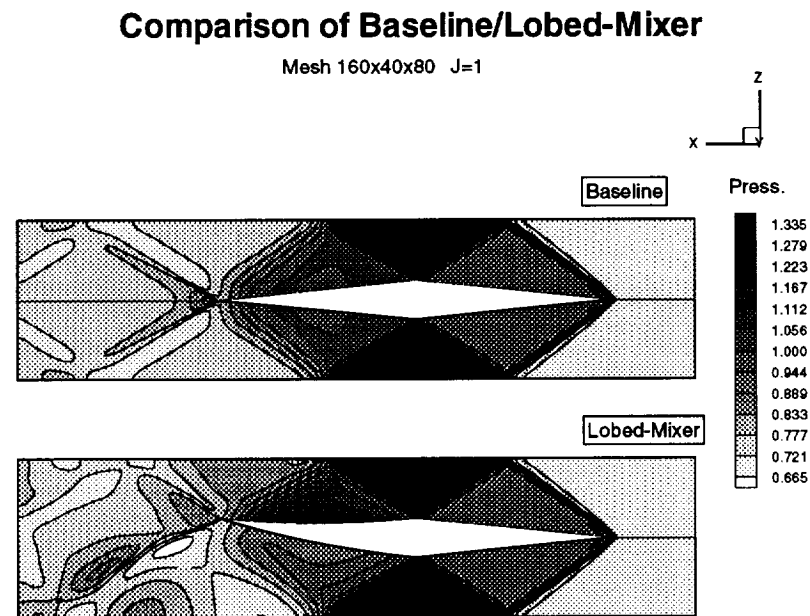
Figure 3.46: Pressure contour at J=1.
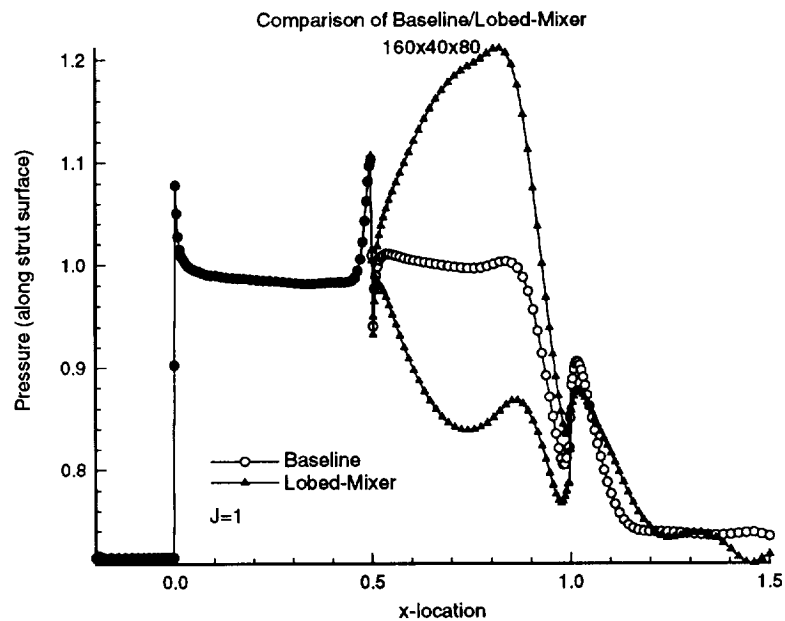
Figure 3.47: Pressure along strut surface along J=1.

Comparison of Baseline/Lobed-Mixer

Cross-velocity vectors at I=161 (at outlet)
160x40x80

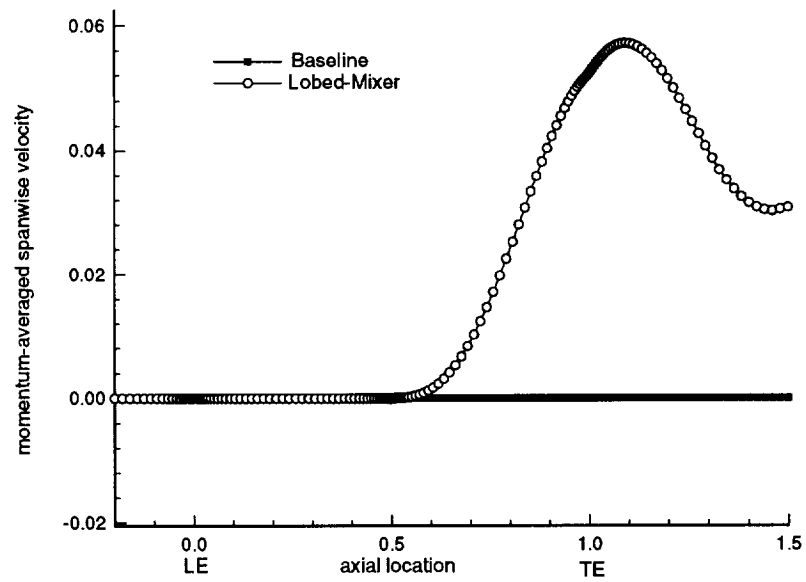Baseline   Lobed-Mixer
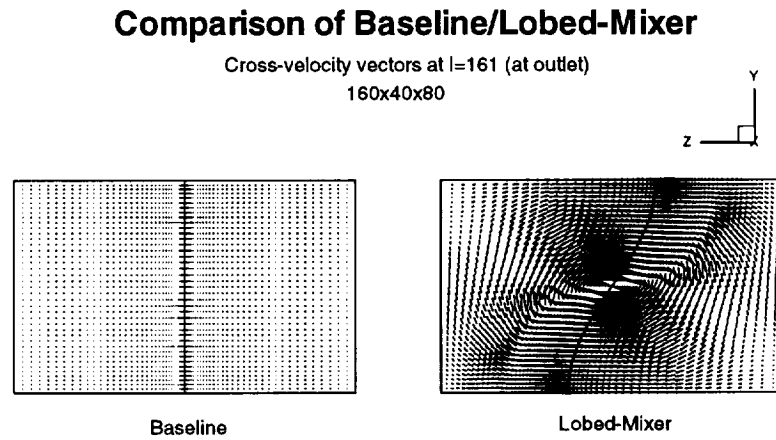
Figure 3.48: Comparison of crossflow velocity vectors.

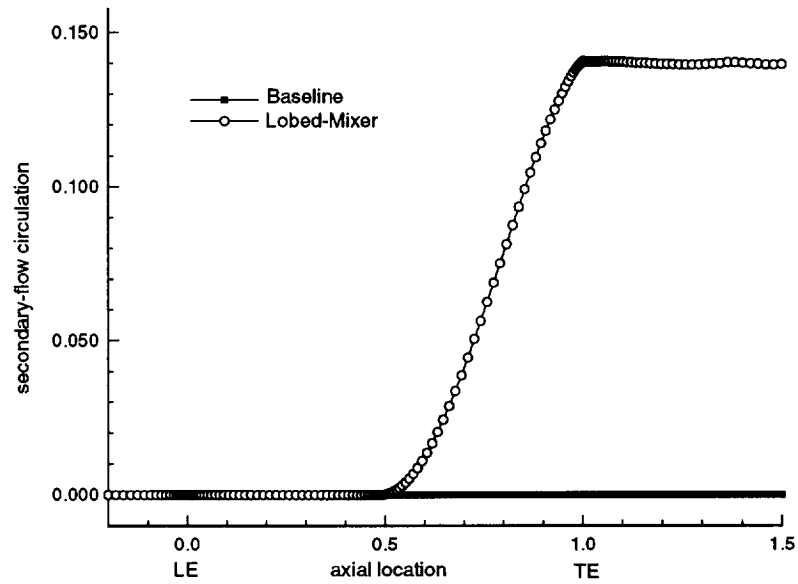Figure 3.49: Momentum averaged spanwise velocity.
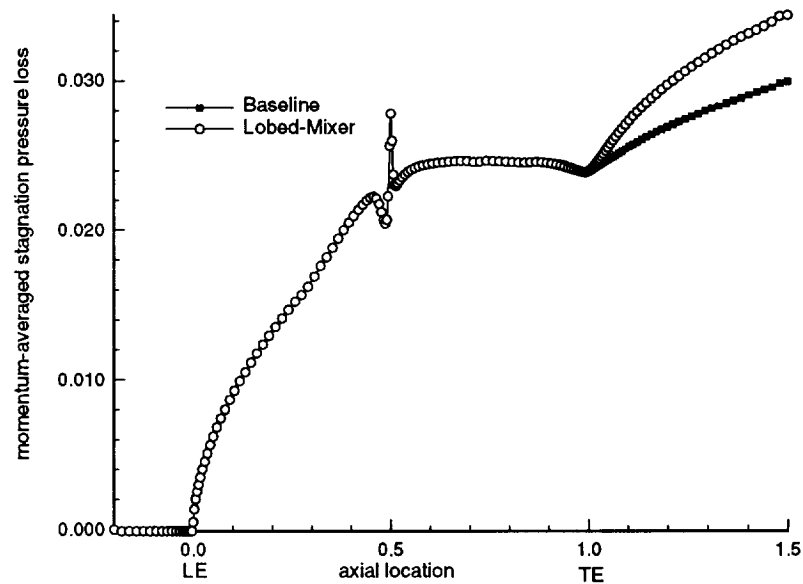
Figure 3.50: Secondary flow circulation.

Figure 3.51: Momentum-averaged stagnation pressure loss.

Chapter 4

Conclusions and Remarks

A computational study was carried out to study the feasibility of using lobed-mixer struts to enhance fuel/air mixing in scramjet engines. The NASA baseline and lobed-mixer struts were first analyzed using an Euler turbomachinery code for a cascaded configuration. Several geometrical configurations were tested for the lobed-mixer, including variations of camber geometry and lobe wavelength and amplitude. A strut with a camber angle at the trailing edge of 12 degrees was chosen for detailed analysis. This particular case was chosen to prevent choking due to flow blockage. Results for two lobes and a camber angle of 12 degrees were very encouraging, revealing strong generation of secondary flows in the flow passage between and behind the struts. For example, the cross-flow velocity magnitude at 50% chord downstream was roughly 10% of the inlet velocity. This gain in secondary flows was achieved with a relatively small loss in drag and total pressure. The loss in stream thrust was 0.31% and 0.77% for the baseline and lobed-mixer respectively, and the loss in total pressure was 3.31% and 4.44% for the baseline and lobed-strut respectively. Furthermore, the wake penetration at 50% downstream of the strut trailing edge was significant, suggesting that fuel injection from the strut can penetrate substantially into the airstream.

The second phase of this work was carried out to assess the importance of viscous effects. The newly-developed NASA LARCK code was used for this investigation. The LARCK code is a Reynolds-Averaged Navier-Stokes (RANS) Computational Fluid Dynamics (CFD) code developed for high-speed reacting flows. Therefore, it is

an appropriate code to simulate the cases studied here.

The configuration studied with LARCK was for a single strut with side walls. The NASA baseline and a lobed-mixer strut with a half-wavelength lobe and a trailing edge camber angle of 12 degrees were studied. For an inflow Mach number of 2, the flow does not separate from the strut. The attached boundary layer introduces blockage into the flowpath, which causes a reduction in strut loading and therefore affects the strength of the secondary flow when compared to the Euler solution. However, the decrease in secondary flow due to viscosity is minimal, suggesting that viscous effects are not important when flow separation is not present. For an inflow Mach number of 3, flow separation occurs as the reflected shock from the wall impinges on the strut suction surface near the trailing edge. For this case, it was found that the pressure loading was reduced significantly when compared to the Euler solution, and consequently the strength of the secondary-flow is decreased substantially.

The effects of the Mach number for inviscid flow was studied. Results reveal that the strength of the secondary-flow was significantly higher for the Mach-3 case than for the Mach-2 case. This is due to a larger pressure loading along the strut for the Mach-3 case (almost twice of the Mach-2 case). Consequently, for supersonic flows, the strength of the secondary flow is a strong function of the Mach number.

Comparisons of the RANS solutions for the NASA baseline case and the hyper-mixer lobed strut demonstrated that the lobed strut produced significant secondary flows, while the baseline case is essentially two-dimensional. The comparison was made at a Mach number of 2, where flow separation is absent. At this flow condition, the results are very similar to the Euler calculations, indicating that the secondary-flow generation mechanism is essentially an inviscid phenomenon. The gain in secondary flows for the lobed strut was achieved with a small increase in drag and stagnation pressure loss. The loss in stream thrust was 0.62% and 1.0% for the baseline and lobed-mixer respectively, and the loss in total pressure was 3.01% and 3.43% for the baseline and lobed-strut respectively.

From the results several points can be stated.

- The streamwise vorticity is generated by a variation in aerodynamic loading

along the span of the lobed mixer strut. The strength of the streamwise vorticity is dependent on the loading of the strut - the higher the loading, the higher the strength of the axial vorticity (Kutta-Joukowsky theorem).

- Viscosity slightly affects the strength of the streamwise vorticity by the introduction of flow blockage, causing a slight decrease in pressure loading along the strut (for non-separated flows).

- For subsonic flow, the work at United Technologies Research Center (UTRC) demonstrated that the circulation of the shed vorticity is proportional to the camber angle. For supersonic flow, we found that the streamwise circulation is also a function of Mach number (or separation distance between the strut and the wall).

Finally, preliminary experiments were carried out to verify the effectiveness of the proposed lobed mixer concept. The tests were performed by Prof. Dimitri Papamoschou at the University of California Irvine using the UCI Supersonic Shear Layer facility. The tests were carried out at freestream Mach numbers of 1.5 and 2.0. Flow visualizations confirmed the existence of large-scale/strong secondary-flows up to several lobe wavelengths downstream of the lobe. In these tests, no measurements were taken to quantify losses. The test results are briefly summarized in Appendix A.

Appendix A

Convergence and mesh sensitivity studies for inviscid and viscous cases are included here, along with the effects of Reynolds numbers and two different turbulence models.

A.1 Inviscid Case

A.1.1 Convergence Study

The size of the mesh used in this study has the following dimension: 113 points in the axial direction (x), 21 points in the spanwise direction (y), and 41 points in the wall to wall direction (z). See figure A.52.

In this subsection a convergence study is carried to determine the minimum order of magnitude drop required to obtain a converged solution. The orders of magnitude studied include 2, 3, 4, and 5 orders of magnitude. The solutions converged to a satisfactory level before 5 orders of magnitude, and therefore 5 orders was not included in this study. Figure A.53 shows the convergence history graph for this solution.

The J=10 spanwise location was selected for inspection of the pressure along the strut surface as shown in figure A.54. It can be easily concluded that 2 orders of magnitude is not a satisfactory level of convergence. The difference in 3 and 4 orders of magnitude is unnoticeable, therefore 3 orders of magnitude is an optimal choice for a converged solution. Other flow variables were also examined at different J locations, however the figures presented here are the ones with larger differences in numerical flow values.

57

A.1.2 Mesh sensitivity Study

In this study three different mesh sizes are used: 112x20x40 (89,600 cells), 144x24x52 (179,712 cells), and 176x32x64 (360,448 cells). Figure A.55 shows the convergence history for the three flow solutions.

Figures A.56 and A.57 show the entropy contour plots at the strut trailing edge plane and at the 50% chord plane downstream of the strut. This figures also represent the location of the trailing vortex shed or "wake". As expected, the wake is thinnest using the fine mesh and thickens as the mesh size is reduced. However, the important thing to note is that the wake-distortion prediction of the three meshes are the same.

Figures A.58 show detailed plots of the pressure along the strut surface at the J=1 location (bottom). These figures indicate again that the coarse mesh solution is slightly different from the other solutions, while the differences for the medium and fine mesh are difficult to notice.

From this study, it is concluded that all three meshes predict the qualitative description of the flowfield of interest to us (i.e. wake distortion and secondary-flow magnitude) to be the same. It is concluded that the medium-size mesh (144x24x52) is a good mesh for engineering flow calculations.

A.2 Viscous Case

A.2.1 Convergence Study

Figures A.59 and A.60 show the computational grid and the convergence history for the viscous calculations.

Figures A.61 shows the pressure along the strut surface at the J=1 spanwise locations for 2.0, 2.5, and 3.5 orders of magnitude. The solution shows insignificant differences for 2.5 and 3.5 orders whereas for 2.0 orders the solution shows a significant change. From the above results, it can be said that around 3.0 orders is needed for a converged solution.

A.2.2 Mesh Sensitivity Study

In this study three different mesh sizes were used, namely 144x32x64 (294,912 cells), 160x40x80 (512,000 cells), and 176x48x96 (811,008 cells).

In Figs. A.62 and A.63, the pressure also shows little variation over mesh size. The strut T.E. shock shows some small variation in strength as the size of the grid is increased. Meaning that a higher value of pressure can be noticed for the fine mesh, over the coarse and medium meshes, but the change is not critical.

Figures A.64, A.65, A.66, and A.67 show velocity-vector plots along the strut surface at the spanwise location where flow separation is most pronounced. Overall, all three meshes predict the presence of flow-separation regions along the suction sections of the strut surface. The coarse mesh predicts a slightly larger separated region than the other two meshes.

From this study, we conclude that all three meshes predict the qualitative description of the flowfield of interest to us (i.e. wake distortion and secondary-flow magnitude) to be the same. It is interesting to note that all three meshes were able to predict large separated flows consistently. We conclude that the medium-size mesh (160x40x80) is adequate for our viscous-flow calculations.

A.3   Effect of Reynolds Number

Two Reynolds numbers were tested, 1.0×10^6 and 1.0×10^7. Figure A.68 shows the pressure along the strut surface. This figure shows that the higher Reynolds-number case produces more lift than the lower Reynolds-number case, suggesting that the former case will result in stronger shed vorticity. Inspections of the flow solutions reveal that the flow-separation regions are reduced as the Reynolds number is increased.

Figure A.69 illustrate the static pressure contours, indicating that the trailing-edge shock is stronger for the 1.0×10^7-Reynolds number case than the 1.0×10^6-Reynolds number case.

Figures A.70 and A.71 illustrate the velocity profiles near the strut surface. The figures show a clear separation of the boundary layer. They also reveal that for the

lower Reynolds number, separation occurs earlier, and the different thickness of the viscous layers can be noticed immediately.

A.4 Effect of Turbulence Model

Two recently developed state-of-the-art turbulence models available in the LARCK code were tested, namely the two-equation model of Menter (NASA-ARC) and the Reynolds stress model of Gatski and Speziale (NASA-LaRC).

Figure A.72 indicates that the Gatski-Speziale model predicts a lower lift on the strut, suggesting that the intensity of secondary flow is lower. Figure A.72 also indicates that the two models predict nearly the same solutions for unseparated flows (i.e. pressure side of strut). Figures A.73 and A.74 show large differences in velocity profiles near the strut surface. The separation for the Menter case occurs very late, and the amount of flow separation is significantly reduced to about 2/3 the physical size with respect to the Gatski-Speziale case. Figures A.75-A.78 show plots of cross-flow velocity vectors. These figures show that overall velocity fields are similar. However, Figs. A.75 and A.76 indicate that the Gatski-Speziale model predicts the presence of secondary streamwise vortices along the suction sides of the strut (i.e. in the separated flow regions), where as the Menter model predicts much weaker secondary streamwise vortices at the strut trailing edge. These differences are probably due to the differences in size of the predicted separated-flow regions by these two models.

A.5 Comparison of LARCK code and 3D Euler code for turbomachines

In the AIAA paper no. 95-2449 entitled "Numerical Study of Lobed-Mixer Fuel-Injection Strut in Scramjet Engine," a 3D Euler code developed for turbomachines is used to assess the effectiveness of this hypermixer concept. This Euler solver employs the original finite-volume Runge-Kutta time-stepping scheme proposed by

Jameson et al. for transonic flows in 1981. The algorithm is equivalent to a central-difference scheme with added scalar artificial viscosity on a uniform rectangular mesh. Consequently, this is not an algorithm of choice for supersonic flows with strong shock waves. Nevertheless, since we already carried out inviscid flow simulations with this code, we have run the LARCK code on the same grid to check the results.

Figures A.79 and A.80 show a comparison of the pressure field on the J=1 plane, and Fig. Overall, the two codes agree very well. As expected, the upwind TVD algorithm of LARCK yields much better shock calculation than our Euler code (i.e low level of oscillations in the LARCK solution).

Figures A.81 and A.82 show predictions of the spanwise velocity V_y at the trailing-edge and outflow axial planes, respectively. This figure indicates that the overall level of spanwise velocity agrees very well at the trailing edge (about 10% of freestream velocity), while the LARCK code predicts a slightly lower level of spanwise velocity at the outflow boundary (about 7% of freestream velocity).

A.6 Preliminary Experimental Test Results

Preliminary experimental verification of the proposed lobed mixer concept was carried out. The tests were performed by Prof. Dimitri Papamoschou at the University of California Irvine in the Supersonic Shear Layer Facility shown in Fig. A.83 [17]. Figure A.84 shows a 3D view of the lobed mixer strut in the test section. A supersonic airstream enters the test section on the upper side of the lobed mixer, while a air/acetone mixture enters the test section on the lower side at the same Mach number. Flow visualizations were carried out at constant axial planes at different downstream locations. Figure A.85 clearly shows the presence of a large-scale vortex (clockwise direction) which displaces fluids from the upper stream toward the lower test section and vice-versa at several crossflow planes for the Mach-1.5 case. Figure A.86 shows similar results for the Mach-2 case. Figure A.87 shows the baseline and lobed-mixer comparisons for the Mach-2 case. The figure reveals the formation of a vortex for the lobed-mixer case several lobe wavelengths downstream of the strut

trailing edge. The baseline case clearly doesn't generate any streamwise vorticity, and the mixing process is predominantly two-dimensional (i.e. shear-induced mixing with normal vorticity). In this preliminary work, no detailed measurements were carried out to quantify flow separation and losses. However, static pressure measurements downstream of the lobe confirmed that the flow did not choke in the test section.
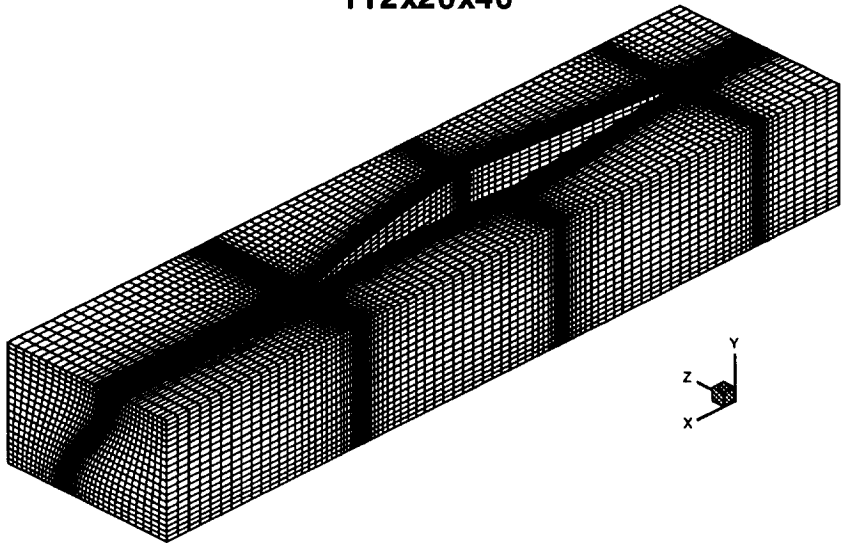
Mesh sensitivity study for Euler solution

112x20x40

Figure A.52: Mesh used for Euler convergence study
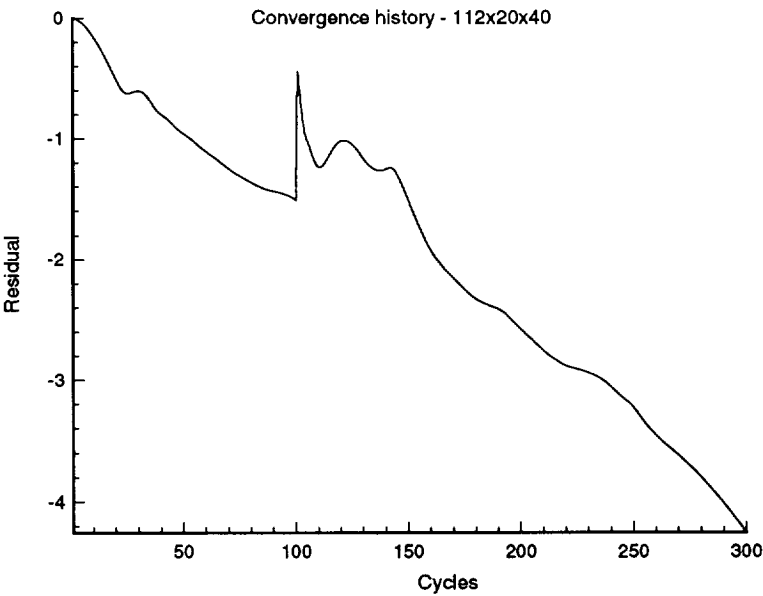
Figure A.53: Convergence history
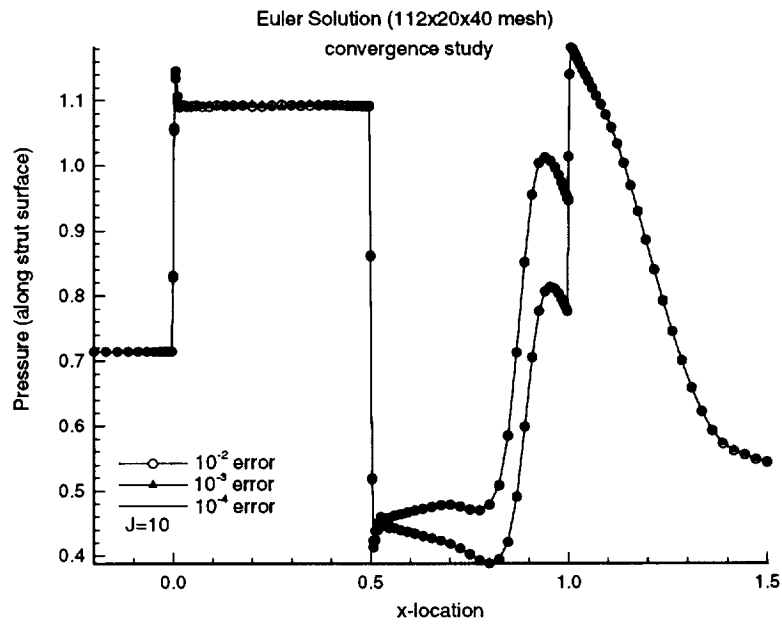
Figure A.54: Pressure along strut surface
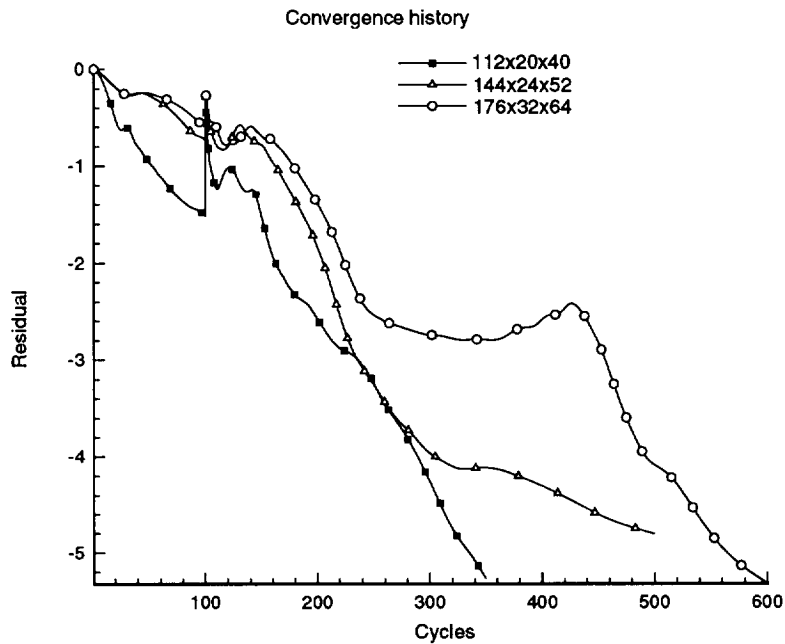
Figure A.55: Convergence history

Mesh sensitivity study for Euler solution

(strut trailing edge)
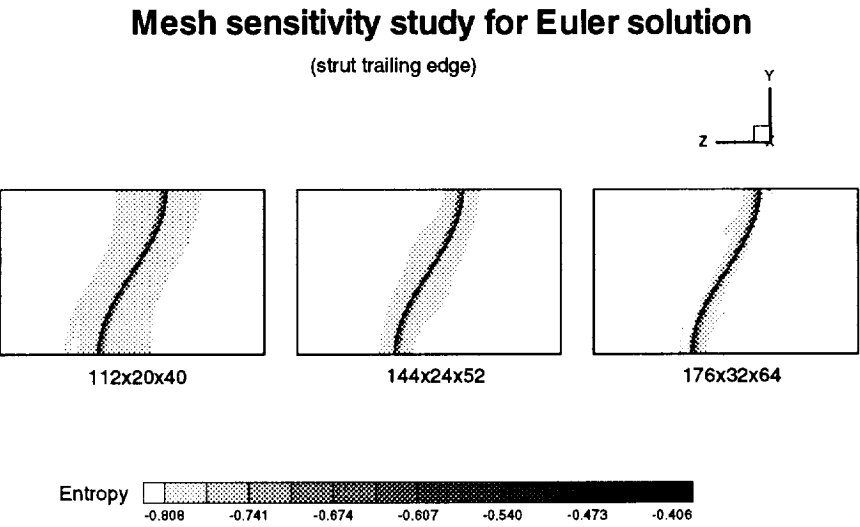
Figure A.56: Entropy at strut T.E.

Mesh sensitivity study for Euler solution

(50% chord downstream)
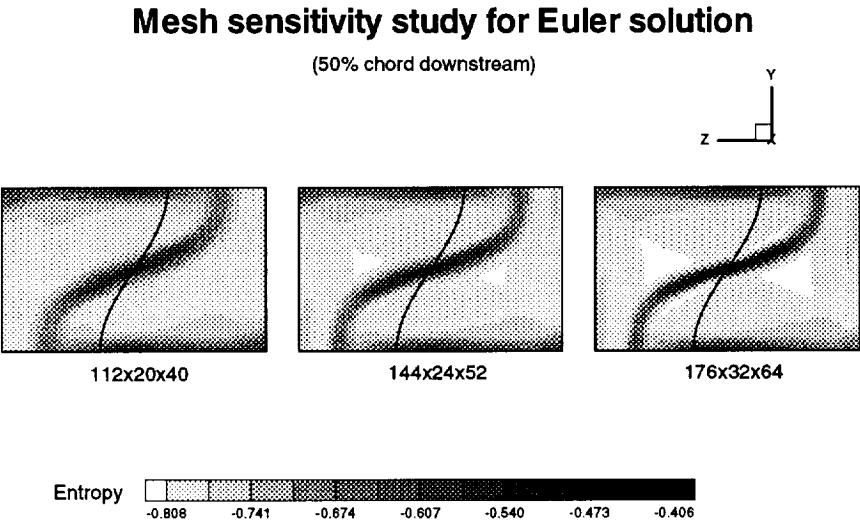
Figure A.57: Entropy at outlet
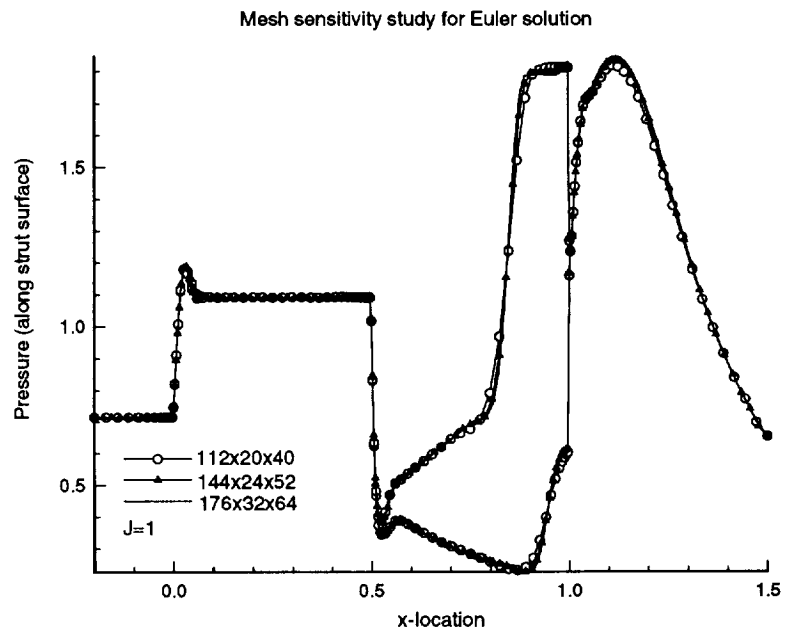
Figure A.58: Pressure along strut surface
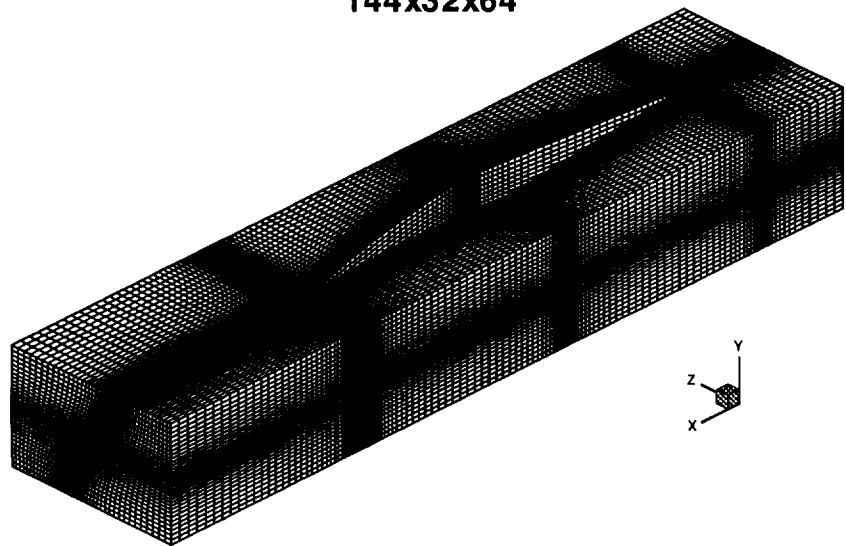
Figure A.59: Viscous mesh for convergence study
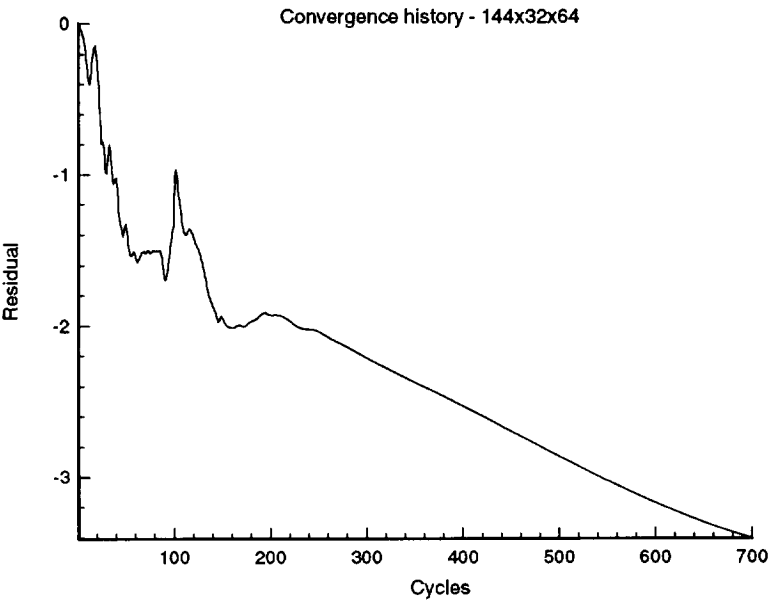
Figure A.60: Convergence history
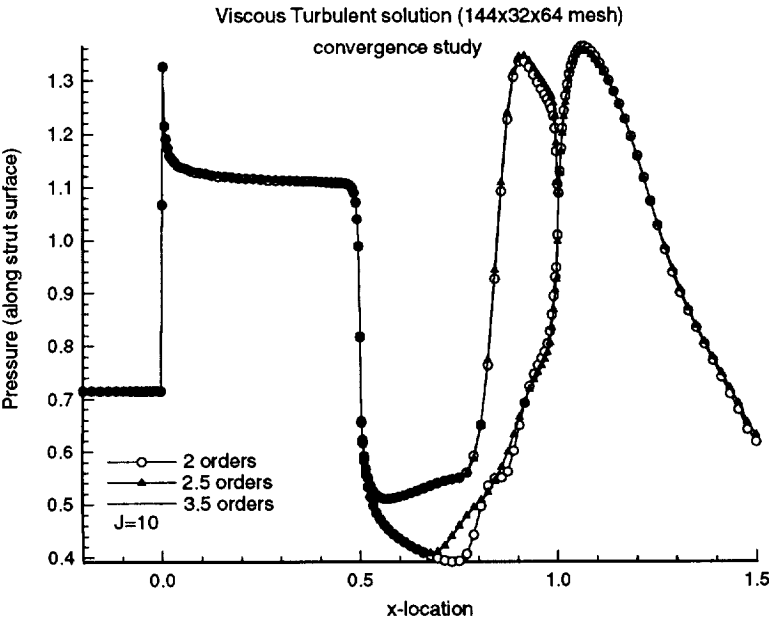
Figure A.61: Pressure along strut surface

Mesh sensitivity study for Viscous solution

J=1
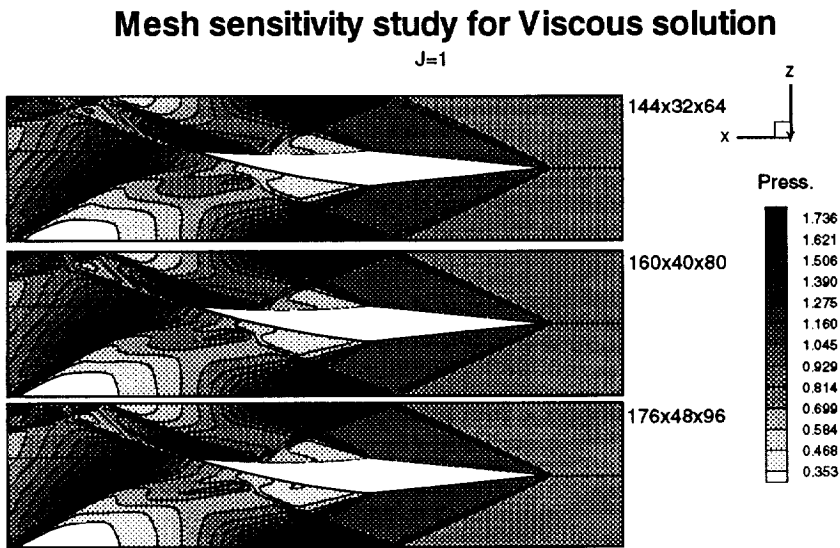
Figure A.62: Pressure at J=1 plane
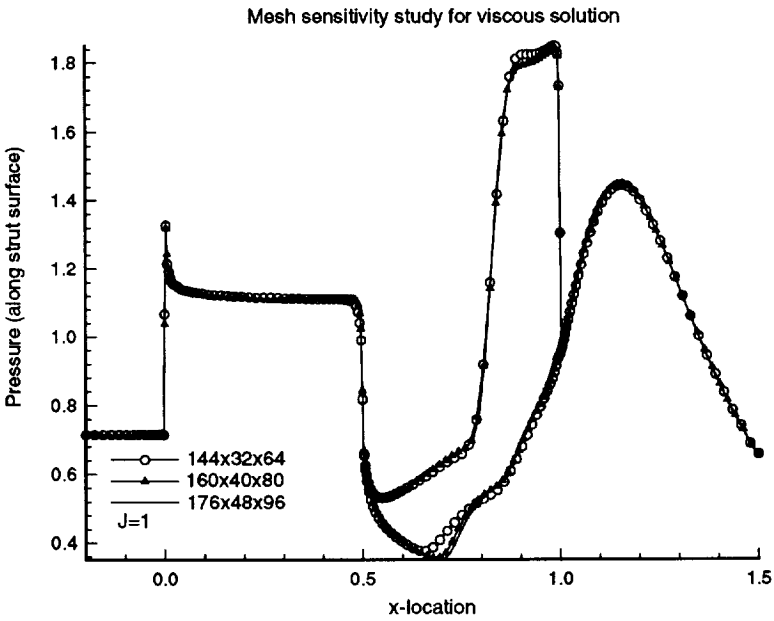
Figure A.63: Pressure along strut surface

Mesh sensitivity study for Viscous solution

Separation region   J=1
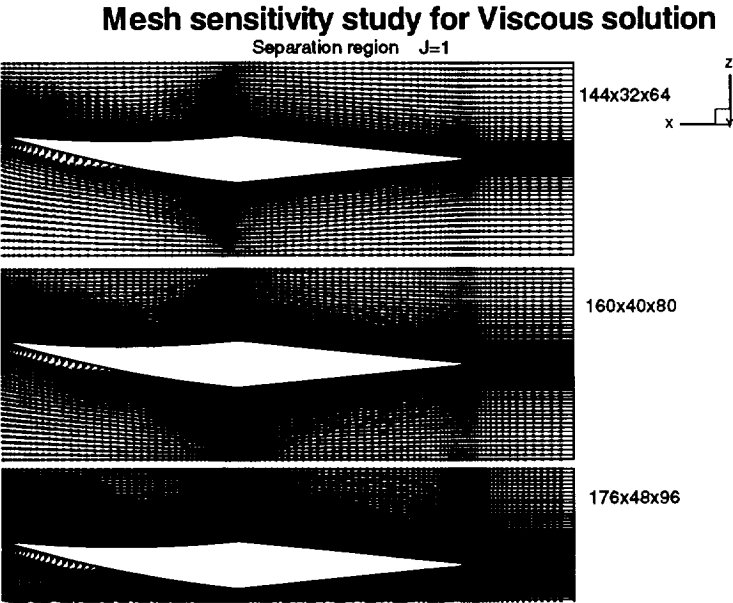
Figure A.64: Velocity vectors

Mesh sensitivity study for Viscous solution

Separation region close-up for 144x32x64
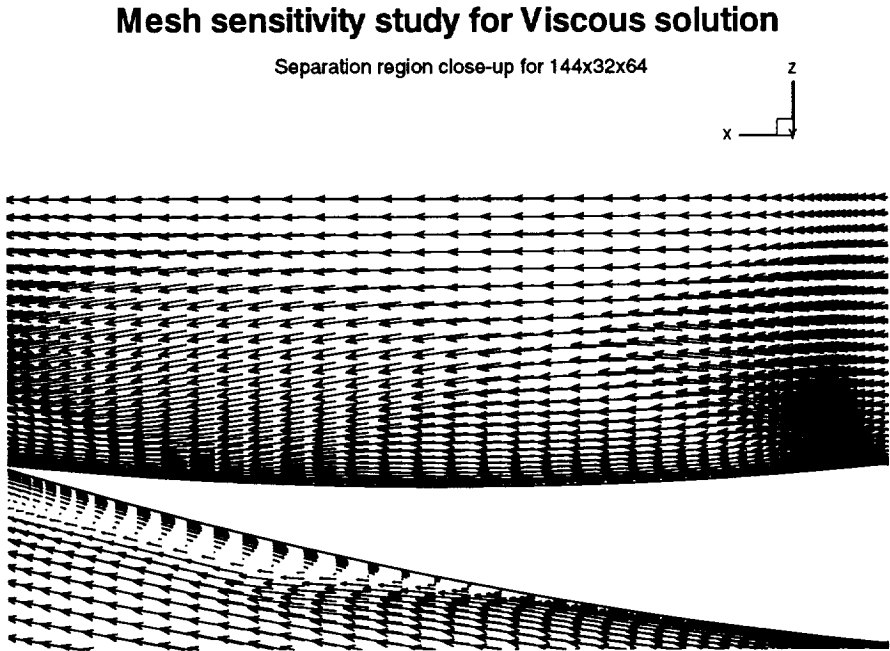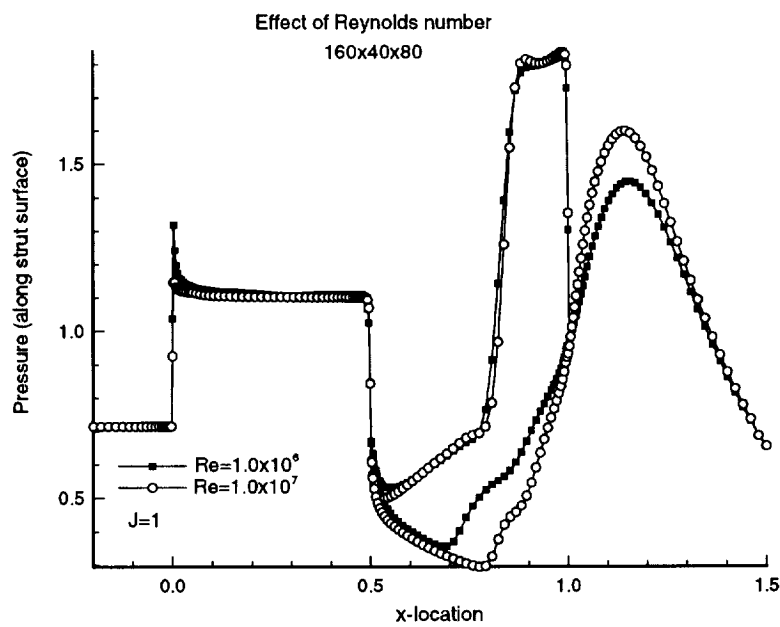

Figure A.65: Velocity vectors close up - 144x32x64

Mesh sensitivity study for Viscous solution

Separation region close-up for 160x40x80
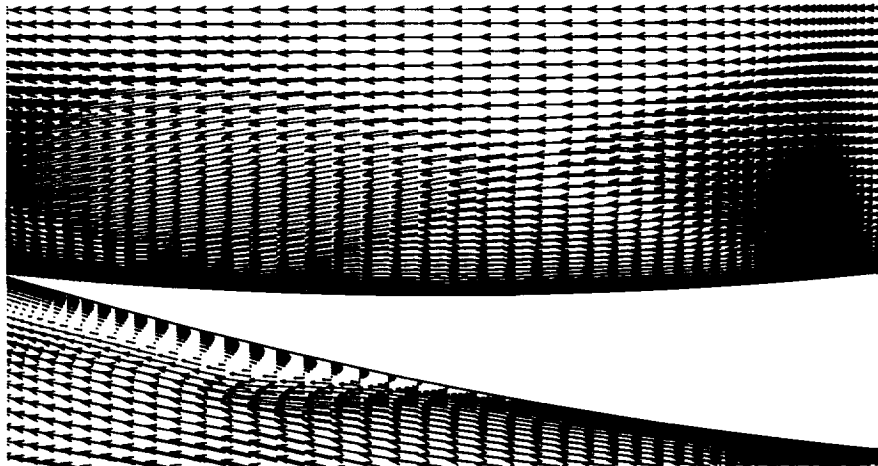
Figure A.66: Velocity vectors close up - 160x40x80

Mesh sensitivity study for Viscous solution

Separation region close-up for 176x48x96
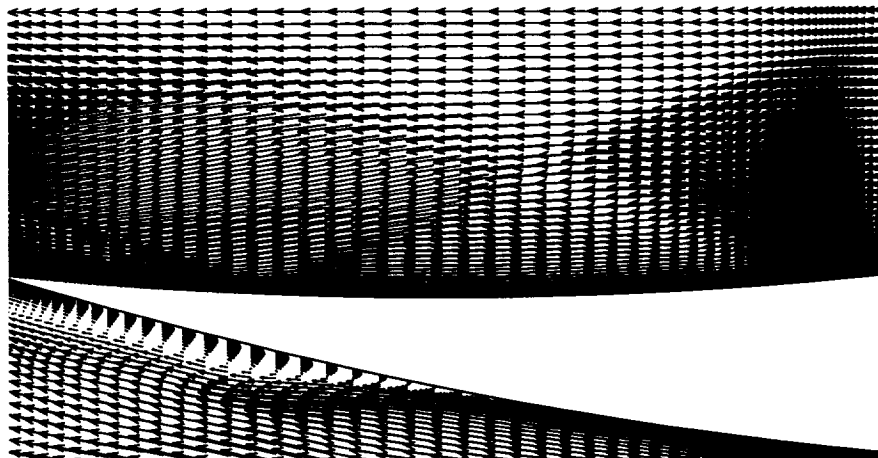
Figure A.67: Velocity vectors close up - 176x48x96

Figure A.68: Pressure along strut surface

Effect of Reynolds Number
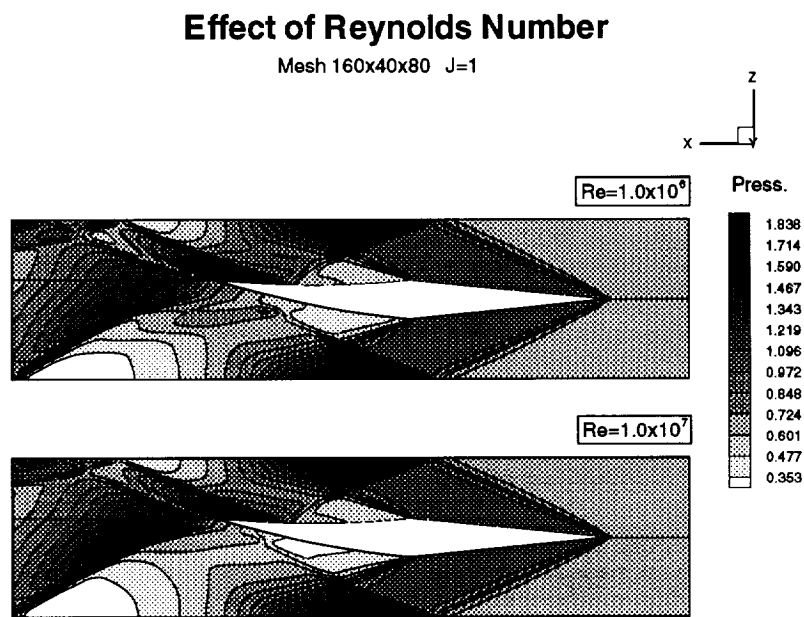
Mesh 160x40x80   J=1

Figure A.69: Pressure at J=1
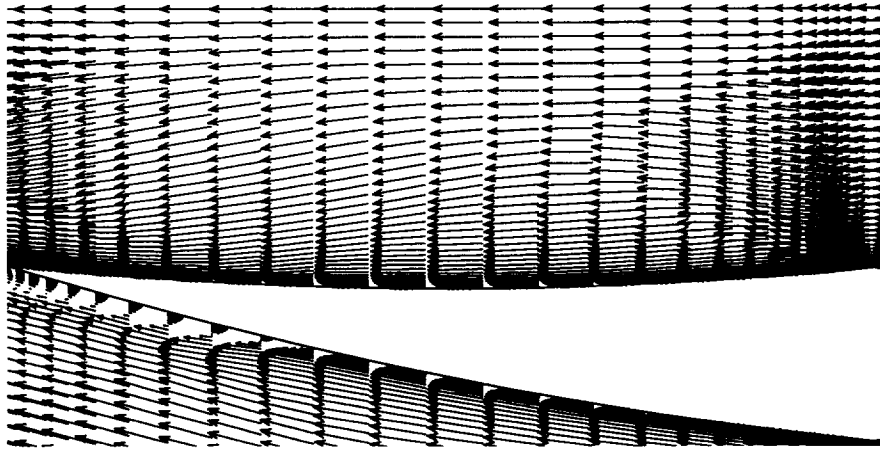
Effect of Reynolds Number

Mesh 160x40x80 J=1
Re=1.0x10^7

Figure A.70: Velocity vectors at J=1
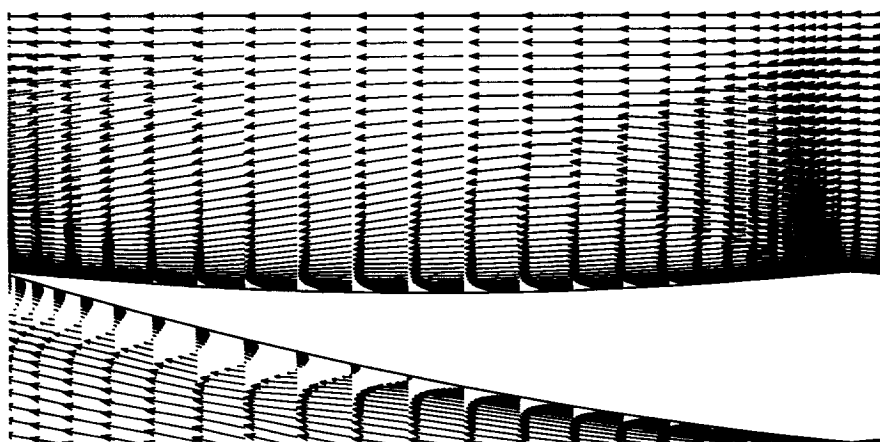
Effect of Reynolds Number

Mesh 160x40x80 J=1
Re=1.0x10^6

Figure A.71: Velocity vectors at J=1
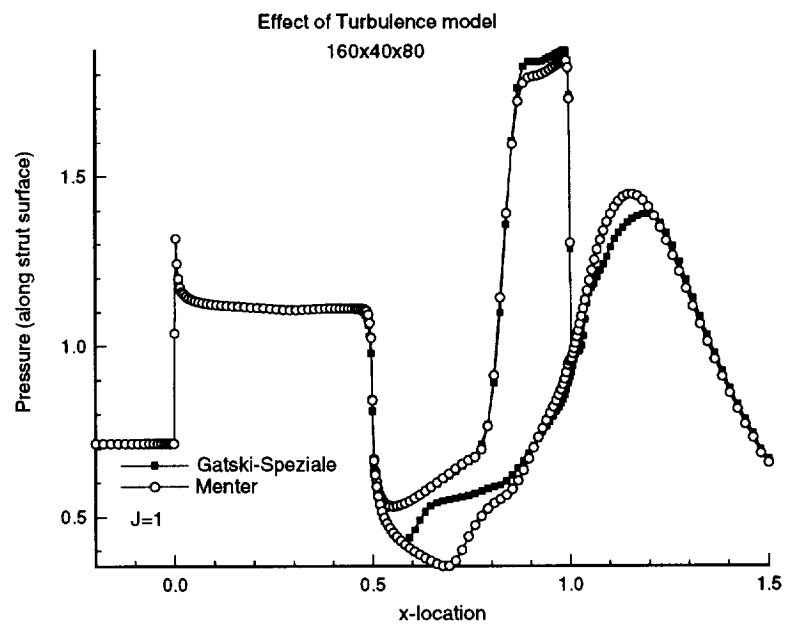
Figure A.72: Pressure along strut surface
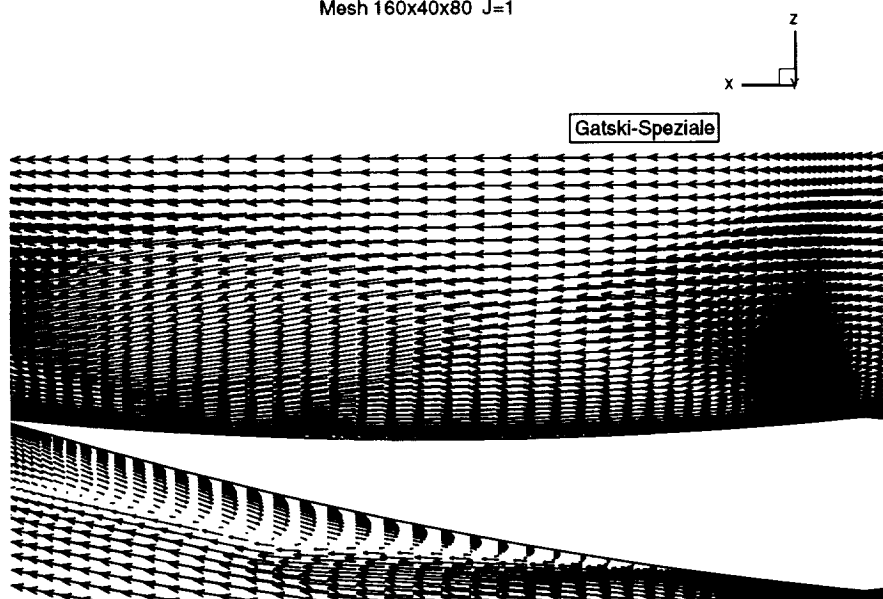
Effect of turbulence model

Mesh 160x40x80 J=1

Gatski-Speziale

Figure A.73: Separation region close-up at J=1
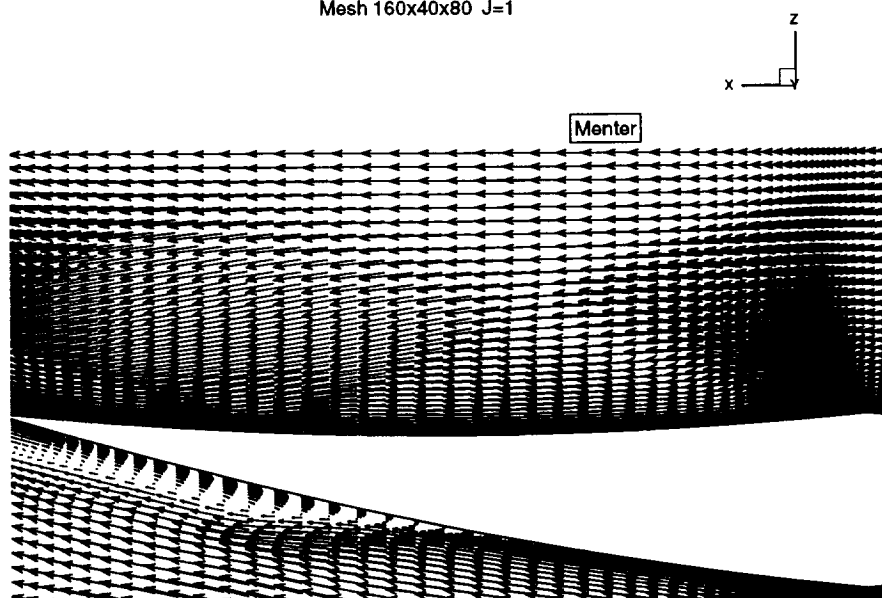
Effect of turbulence model

Mesh 160x40x80 J=1

Menter

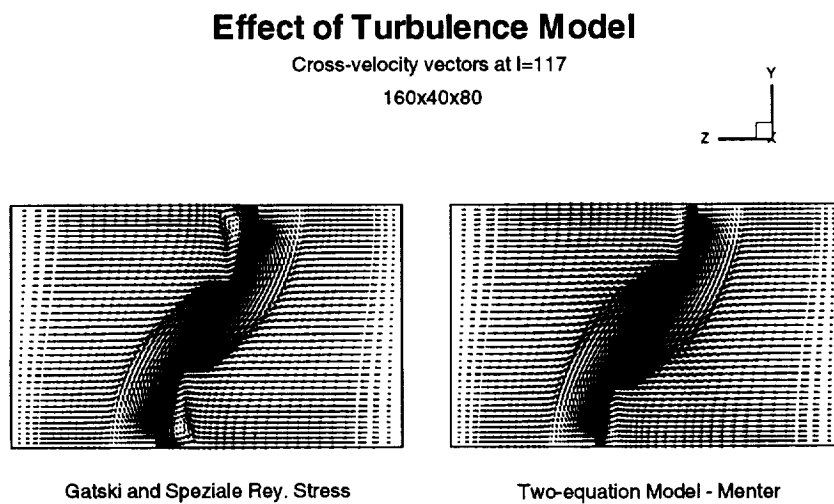Figure A.74: Separation region close-up at J=1

Effect of Turbulence Model

Cross-velocity vectors at I=117

160x40x80

Gatski and Speziale Rey. Stress

Two-equation Model - Menter

Figure A.75: Cross-velocity vectors at strut T.E. - I=117

Effect of Turbulence Model

Cross-velocity vectors at I=134

160x40x80

Gatski and Speziale Rey. Stress

Two-equation Model - Menter
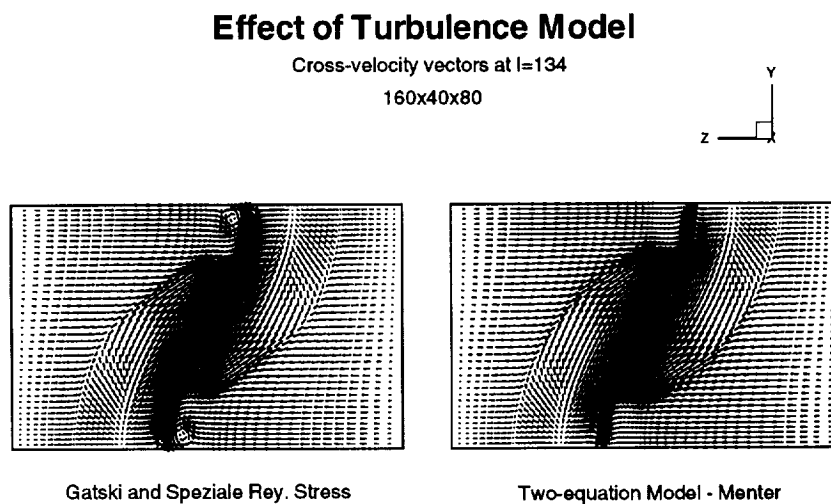
Figure A.76: Cross-velocity vectors at I=134

Effect of Turbulence Model

Cross-velocity vectors at I=147

160x40x80

Gatski and Speziale Rey. Stress   Two-equation Model - Menter
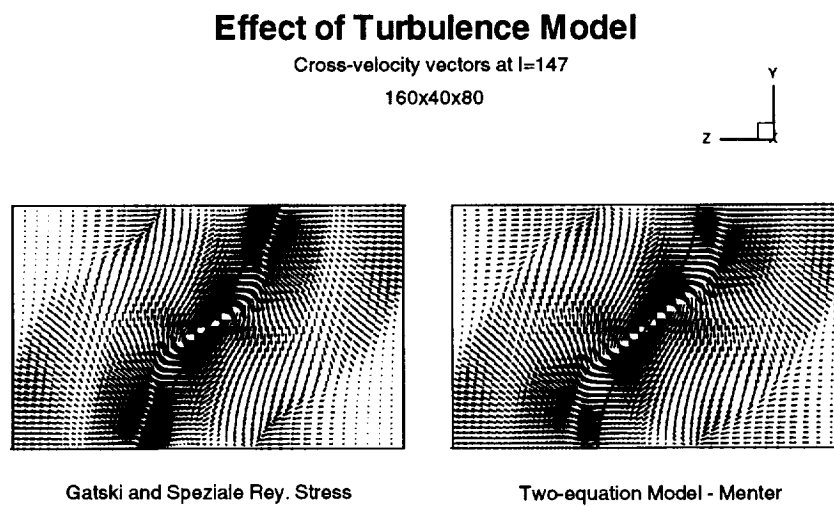
Figure A.77: Cross-velocity vectors at I=147

Effect of Turbulence Model

Cross-velocity vectors at I=161

160x40x80

Gatski and Speziale Rey. Stress   Two-equation Model - Menter
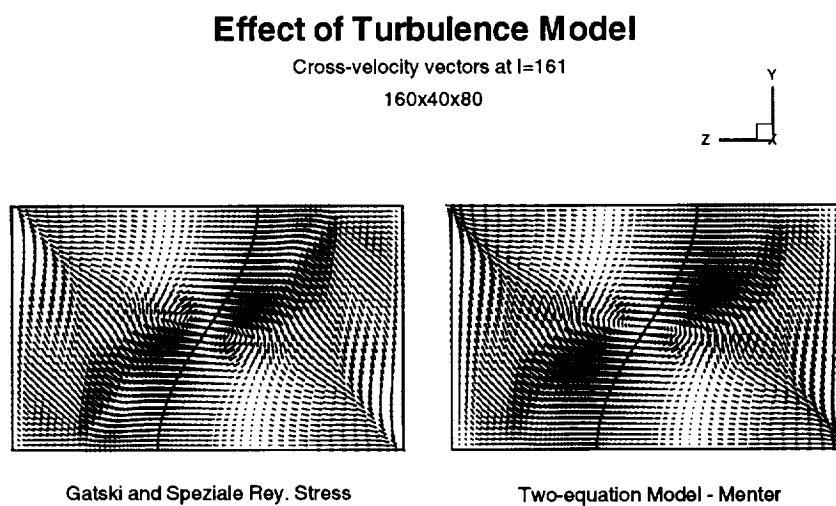
Figure A.78: Cross-velocity vectors at outlet - I=161

AIAA 95-2449 solution

Mesh 176x60x28

z
x

J=1

Pressure

0.600 0.803 1.007 1.210 1.413 1.617 1.820
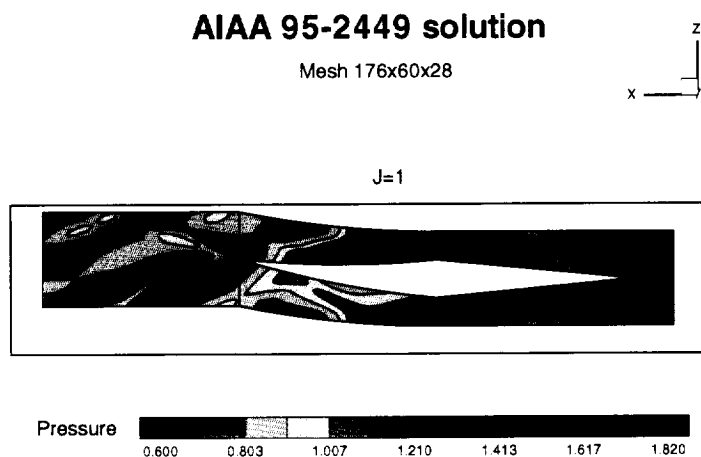
Figure A.79: Pressure at J=1

LARCK solution

Mesh 176x60x28

z
x

J=1

Pressure

0.600 0.803 1.007 1.210 1.413 1.617 1.820
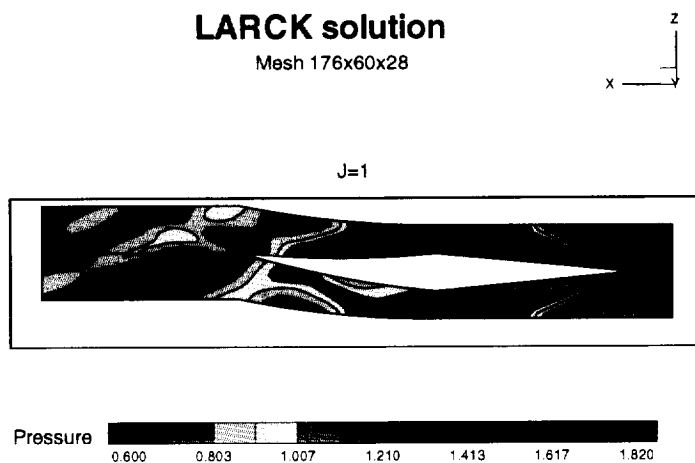
Figure A.80: Pressure at J=1

AIAA 95-2449 solution

Mesh 176x60x28
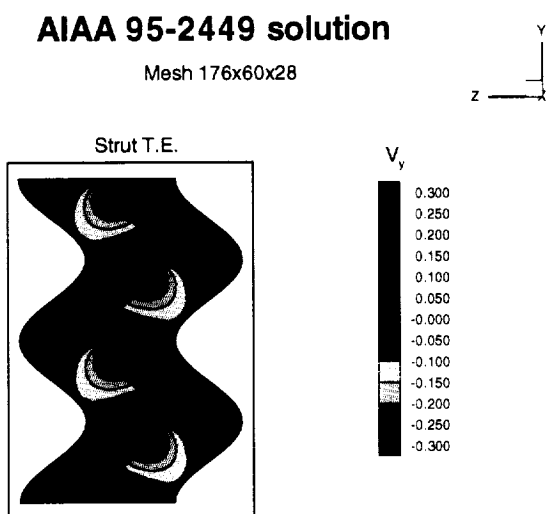
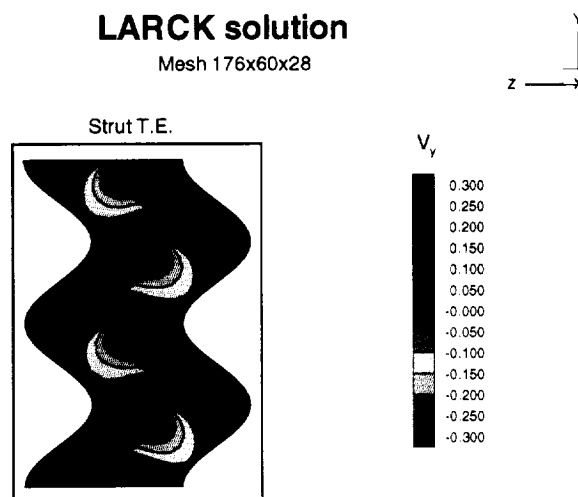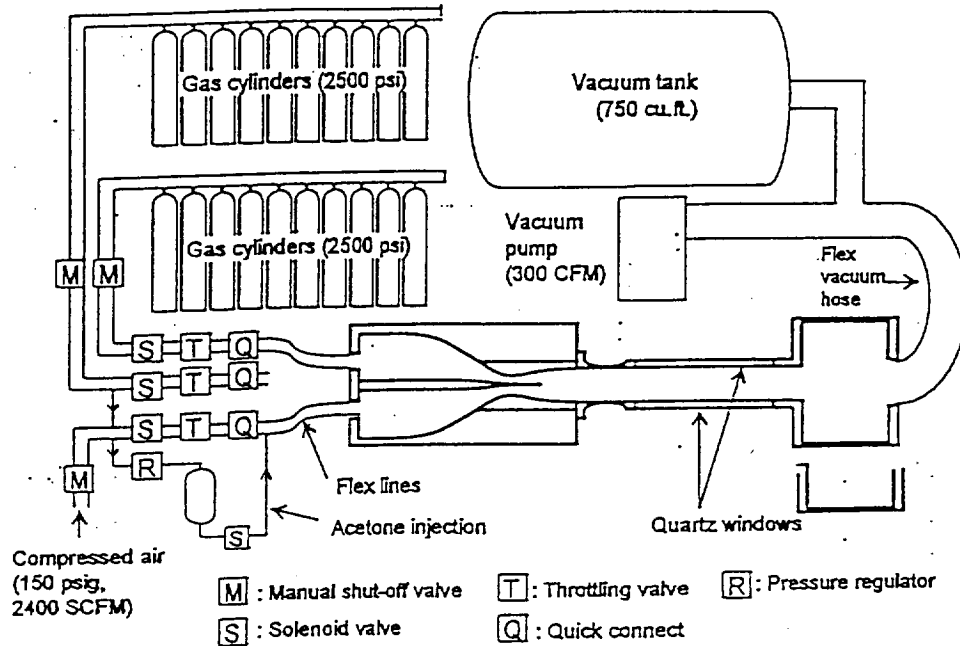Figure A.81: Spanwise velocity at strut T.E.

LARCK solution

Mesh 176x60x28

Figure A.82: Spanwise velocity at strut T.E.

UCI SUPERSONIC TURBULENCE LABORATORY

Supersonic Shear Layer Facility

CAPABILITIES:
MACH NUMBERS: 0 TO 4 (currently available: subsonic, 1.5, 2.0, 3.0)
GASES: any non-toxic, non-flammable gas (Air, He, Ar, SF6, CO2, etc.)
TEST-SECTION PRESSURE: up to atmospheric
TOTAL PRESSURES: up to 10 atm
REYNOLDS NUMBERS: up to 10E6 based on shear-layer thickness
TEST SECTION DIMENSIONS: 2.5"W, 1.5"H, 12"L
TEST SECTION DESIGN: top and bottom walls can be deflected to adjust pressure gradient. Quartz windows installed on all 4 walls

INSTRUMENTATION:
Planar laser-induced fluorescence in single or double-exposure mode
Nanosecond schlieren photography (6" beam dia., CCD camera)
Spectrum Measurement Technique
Total and static pressure transducers
Fully automated control and data acquisition

MAJOR DIAGNOSTIC EQUIPMENT:
Two Continuum Surelite II Nd:Yag Lasers
Photometrics Star I CCD camera (12-bit)
Princeton Instruments Intensified CCD camera (16-bit)
Xenon Nanolamp nanosecond spark source
Oriel He-Ne laser
PC 486 and Pentium computers

For more information please contact:
Prof. Dimitri Papamoschou
Dept. of Mechanical and Aerospace Engr.
University of California, Irvine
Irvine, CA 92697-3975
Tel: (714) 824-8590
Fax: (714) 824-8585
E-mail: dpapamos@uci.edu

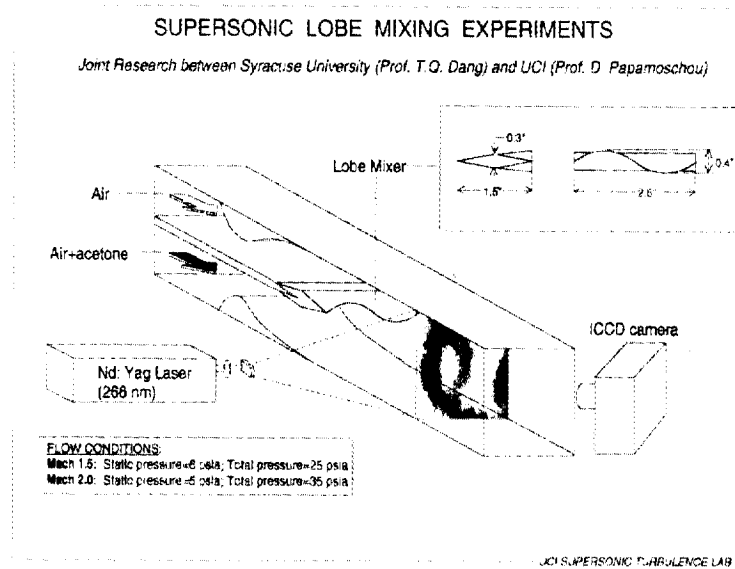Figure A.83: Supersonic shear layer facility at UCI.

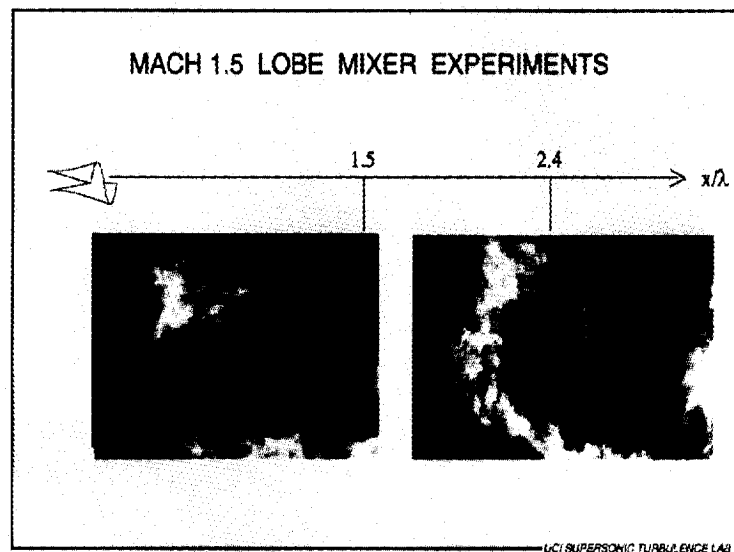Figure A.84: 3D view of the lobed mixer strut in the test section.

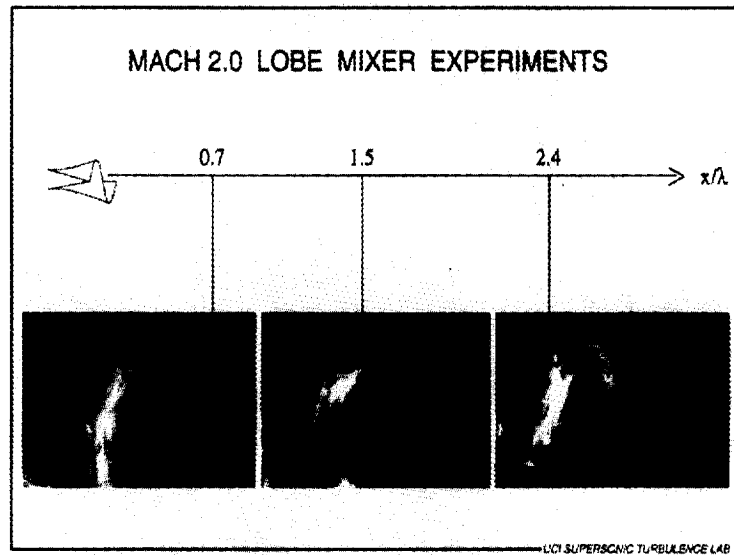Figure A.85: Experimental results for Mach 1.5 lobe mixer case.

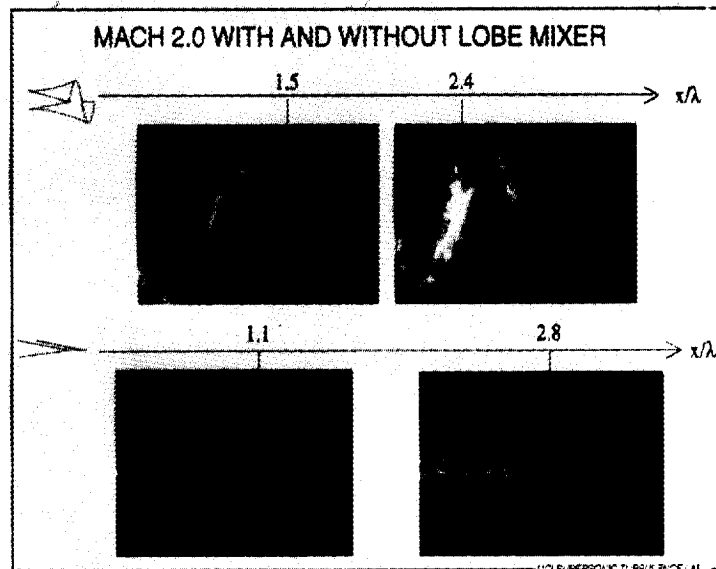Figure A.86: Experimental results for Mach 2.0 lobe mixer case.

Figure A.87: Experimental results for Mach 2.0 lobe mixer and baseline cases.

Bibliography

[1] Barber, T.J., Muller, G.L., Ramsay, S.M., and Murman, E.M., "Three Dimensional Inviscid Flow in Mixers, Part I: Mixer Analysis Using a Cartesian Grid," AIAA Journal of Propulsion and Power, vol. 2, no. 3, 1986, pg. 275.

[2] Brown, G.L. and Roshko, A., "On Density Effects and Large Structure in Turbulent Mixing Layers," *J. Fluid Mech.*, vol. 64, no. 4, 1974, pp. 775-816.

[3] Bulman, M.J., Siebenhaar A., "Rocket Based Combined Cycle Propulsion for Space Launch," International Astronautical Federation Paper 95-S.5.02.

[4] Dang, T.Q., "Inverse Method for Turbomachine Blades Using Shock-Capturing Techniques," AIAA Paper 95-2465, 1995.

[5] Drummond, J.P., "Supersonic Reacting Internal Flow Fields," Numerical approaches to Combustion Modeling, Oran, E.S. and Boris, J.P., eds., AIAA Progress in Aeronautics and Astronautics, 1991.

[6] Elliot, J.K., Manning, T.A., Qiu, Y.J., Greitzer, E.M., Tan, C.S. and Tillman, T.G., "Computational and Experimental Studies of Flow in Multi-Lobed Forced Mixers," AIAA Paper 92-3568, 1992.

[7] Gutmark, E.J., Schadow, K.C. and Yu, K.H., "Mixing Enhancement in Supersonic Free Shear Flows," *Ann. Rev. Fluid Mech.*, vol. 27, 1995, pp. 375-417.

[8] Jameson, A., Schmidt, W. and Turkel, E., "Numerical Solution of the Euler Equations by Finite Volume Methods Using Runge-Kutta Time-Stepping Schemes," AIAA paper no. 81-1259, 1981.

[9] Korte, J.J., Singh, D.J., Kumar, A. and Auslender, A.H., "Numerical Study of the Performance of Swept, Curved Compression Surface Scramjet Inlets," *Journal of Propulsion and Power*, vol. 10, no. 6, 1994, pp. 841-847.

[10] Kumar, A., Bushnell, D.M. and Hussaini, M.Y., "Mixing Augmentation Technique for Hypervelocity Scramjets," *Journal of Propulsion and Power*, 1991, pp. 514-522.

[11] Kumar, A., Singh, D. J. and Trexler, C. A., "Numerical Simulation of Flow Through a Two-Strut Scramjet Inlet," *Journal of Propulsion and Power*, vol. 5, no. 3, 1992, pp. 341-345.

[12] Kumar, A., Singh, D. J. and Trexler, C. A., "A Numerical Study of the Effects of Reverse Sweep on a Scramjet Inlet Performance," *Journal of Propulsion and Power*, vol. 8, no. 3, 1992, pp. 714-719.

[13] McCormick, D.C., "Vortical and Turbulent Structure of Planar and Lobed Mixer Free-Shear Flows," Ph.D. Thesis, University of Connecticut, 1992.

[14] Northam, G.B., Greenberg, I., Byington, C.S. and Capriotti, D.P., "Evaluation of Parallel Injector Configurations for Mach 2 Combustion," *Journal of Propulsion and Power*, vol. 8, no. 2, 1992, pp. 491-499.

[15] Papamoschou, D. and Roshko, A., "The Compressible Turbulent Shear Layer: An Experimental Study," *J. Fluid Mech.*, vol. 197, 1988, pp. 453-477.

[16] Paterson, R. W., "Turbofan Mixer Nozzle Flow Field - A Benchmark Experimental Study," *Journal of Engineering for Gas Turbine and Power*, vol. 106, 1984, pp. 692-698.

[17] Papamoschou, D., Bunyajitradulya, A., "Evolution of large eddies in compressible shear layers." *Physics of Fluids*, 1997 Mar., V9 N3:756-765.

[18] Singh, D. J., Trexler, C. A. and Hudgens Young, J. A., "Three-Dimensional Simulation of a Translating Strut Inlet," *Journal of Propulsion and Power*, vol. 10, no. 2, 1994, pp. 191-197.

[19] Skebe, S.A., Paterson, R.W. and Barber, T.J., "Experimental Investigation of Three-Dimensional Forced Mixer Lobe Flow Fields," AIAA Paper 88-3785, 1988.

[20] Tillman, T.G., Patrick, W.P. and Paterson, R.W., "Enhanced Mixing of Supersonic Jets," *Journal of Propulsion and Power*, vol. 7, no. 6, 1991, pp. 1006-1014.

[21] Trexler, C. A., "Design and Performance at a Local Mach Number of 6 and an Inlet for an Integrated Scramjet Concept," NASA TN D-7944, 1975.

Vita

NAME OF AUTHOR: Mario Felipe Campuzano

PLACE OF BIRTH: Kansas City, MO. USA

DEGREES   B.S. in Mechanical Engineering, State University of New
AWARDED: York at Buffalo, 1994. – B.S. in Aerospace Engineering,
                 State University of New York at Buffalo, 1994.